International Journal of Earth Sciences

Syn-deformational melt percolation through a high-pressure orthogneiss and the exhumation of a subducted continental wedge (Orlica-Śnieżnik Dome, NE Bohemian Massif)

--Manuscript Draft--

Manuscript Number:	
Full Title:	Syn-deformational melt percolation through a high-pressure orthogneiss and the exhumation of a subducted continental wedge (Orlica-Śnieżnik Dome, NE Bohemian Massif)
Article Type:	Original Paper
Keywords:	HP-granitic orthogneiss; petrological modelling; melt percolation; exhumation
Corresponding Author:	Carmen Aguilar, Ph.D Ceska Geologicka Sluzba Prague, Prague CZECH REPUBLIC
Corresponding Author Secondary Information:	
Corresponding Author's Institution:	Ceska Geologicka Sluzba
Corresponding Author's Secondary Institution:	
First Author:	Carmen Aguilar, Ph.D
First Author Secondary Information:	
Order of Authors:	Carmen Aguilar, Ph.D
	Pavla Štípská
	Francis Chopin
	Karel Schulmann
	Pavel Pitra
	Prokop Závada
	Pavlína Hasalová
	Jean-Emmanuel Martelat
Order of Authors Secondary Information:	
Funding Information:	
Abstract:	High-pressure migmatitic orthogneiss of the south-eastern Orlica–Śnieżnik Dome (NE Bohemian Massif) shows relics of a shallow-dipping foliation, reworked by upright folds and a mostly pervasive N-S trending subvertical axial planar foliation. Based on macroscopic observations, a gradual transition from augen-banded orthogneiss through banded orthogneiss, to schlieren and nebulitic migmatites was distinguished. All rock types comprise plagioclase, K-feldspar, quartz, white mica, biotite and garnet. The transition is characterized by increasing nucleation of interstitial phases along like-like grain boundaries and by progressive corrosion of recrystallized K-feldspar grains by fine-grained myrmekite. These textural changes are characteristic for syn-deformational grain-scale melt percolation, which is in line with the observed enrichment of the rocks in incompatible elements such as Ba, Sr, Eu, K and Rb suggesting open-system behaviour with melt passing through the rocks. The P – T path deduced from the thermodynamic modelling indicates decompression from ~15−16 kbar and ~650–740 °C to ~6 kbar and ~640 °C. Melt was already present at the P–T peak conditions as indicated by the composition of plagioclase in myrmekite and in interstitial films. The variably re-equilibrated garnet suggests that melt content may have varied along the decompression path, involving successively both melt gain and loss. 6 – 8 km wide zone of vertical foliation and migmatite textural gradients is

	interpreted as vertical crustal-scale channel where the grain-scale melt percolation was associated with horizontal shortening and vertical flow of partially molten crustal wedge en masse.

Syn-deformational melt percolation through a high-pressure orthogneiss and the exhumation of a subducted continental wedge (Orlica-Śnieżnik Dome, NE Bohemian Massif)

Carmen Aguilar[a*], Pavla Štípská[a,b], Francis Chopin[a,b], Karel Schulmann[a,b], Pavel Pitra[a,c], Prokop Závada[d], Pavlína Hasalová[a], Jean-Emmanuel Martelat[e]

[a] *Centre for Lithospheric Research, Czech Geological Survey, Klárov 3, CZ−11821 Prague, Czech Republic*

[b] *École et Observatoire des Sciences de la Terre, Institut de Physique du Globe – CNRS UMR7516, Université de Strasbourg, 1 rue Blessig, F−67084 Strasbourg Cedex, France*

[c] *Université de Rennes, CNRS, Géosciences Rennes - UMR 6118, F-35000 Rennes, France*

[d] *Institute of Geophysics, Academy of Sciences, Boční II/1401, CZ–14131 Prague, Czech Republic.*

[e] *Laboratoire de Géologie de Lyon – CNRS UMR5276, Université Claude Bernard et École Normale Supérieure, F−69622 Villeurbanne, France*

***** *Corresponding author:* carmen.gil@geology.cz (C. AGUILAR)

ABSTRACT

High-pressure migmatitic orthogneiss of the south-eastern Orlica–Śnieżnik Dome (NE Bohemian Massif) shows relics of a shallow-dipping foliation, reworked by upright folds and a mostly pervasive N-S trending subvertical axial planar foliation. Based on macroscopic observations, a gradual transition from augen-banded orthogneiss through banded orthogneiss, to schlieren and nebulitic migmatites was distinguished. All rock types comprise plagioclase, K-feldspar, quartz, white mica, biotite and garnet. The transition is characterized by increasing nucleation of interstitial phases along like-like grain boundaries and by progressive corrosion of recrystallized K-feldspar grains by fine-grained myrmekite. These

textural changes are characteristic for syn-deformational grain-scale melt percolation, which is in line with the observed enrichment of the rocks in incompatible elements such as Ba, Sr, Eu, K and Rb suggesting open-system behaviour with melt passing through the rocks. The *P*–*T* path deduced from the thermodynamic modelling indicates decompression from ~15−16 kbar and ~650–740 °C to ~6 kbar and ~640 °C. Melt was already present at the *P*–*T* peak conditions as indicated by the composition of plagioclase in myrmekite and in interstitial films. The variably re-equilibrated garnet suggests that melt content may have varied along the decompression path, involving successively both melt gain and loss. 6–8 km wide zone of vertical foliation and migmatite textural gradients is interpreted as vertical crustal-scale channel where the grain-scale melt percolation was associated with horizontal shortening and vertical flow of partially molten crustal wedge en masse.

Keywords: H*P*-granitic orthogneiss; petrological modelling; melt percolation; exhumation

INTRODUCTION

Recent petrological and microstructural studies show increased role of interplay between grain-scale melt transfer and deformation in various tectonic settings ranging from Tibetan type channel flow (Finch et al. 2014), continental subduction (Závada et al. 2018), extrusion of subducted crust in continental wedges (Štípská et al. 2019) and in Cordilleran magmatic arc (Stuart et al. 2018). In all these settings melt passes through deforming crust exploiting grain boundaries of felsic granitic protoliths without segregation into veins and dykes typical for metasedimentary migmatites (Collins and Sawyer, 1996; Brown and Solar, 1998; Weinberg, 1999; Vanderhaeghe, 2001). For all the above mentioned studies the typical feature is connection of this pervasive grain-scale flow with ductile shear zones, in particular

with domains characterized by almost isotropic granite-like texture (Hasalová et al. 2008a; Závada et al. 2018). Závada et al. (2018) also suggested that prerequisite of pervasive porous flow of granitic melt is granular cohesion-less grain boundary sliding of relictual parental grains enabling dynamic dilatancy of grain boundaries, typical for ultramylonitic cores of shear zones (Závada et al. 2007; Schulmann et al. 2008; Oliot et al. 2014).

Petrological studies characterizing role of melt for vertical transfer of rocks through crust are scarce, but the existing studies indicate that chemistry of crystallized interstitial melt and compositional variations of minerals can record exhumation of rocks of the order of ~10–20 kilometers (Hasalová et al. 2008b; Štípská et al. 2019). In addition, these studies indicate that dynamically moving melt plays a major role in exhuming large portions of continental crust. Quantitative petrological studies of simultaneously migmatitized and deformed granitoids thus provide unique insight into mechanisms of exhumation of deeply buried crust as proposed already by pioneering works of Hollister (1993) and Brown and Solar (1998).

The Orlica-Śnieżnik Dome (OSD) located at the NE extremity of the Bohemian Massif represents an ideal site where simultaneous deformation and melt transfer can be studied (see Fig. 1). The OSD is part of a continental wedge that shows structural and petrological records of continental subduction followed by vertical extrusion of partially molten deep crust in form of a giant gneiss dome (Chopin et al. 2012a). The extrusion process is characterized by elevation of two antiforms. The western Międzygórze antiform is marked by good preservation of shallow-dipping H*P* subduction fabrics reworked by vertical and localized melt-bearing zones, associated with heterogeneous exhumation of buried rocks (Štípská et al. 2019). In contrast, the eastern and larger Králíky-Śnieżnik antiform shows widespread melting of the crust associated with almost complete reworking of previously subducted rocks in up to 10-kilometer-wide zone of migmatites and granitoids (Chopin et al. 2012a; Lehmann et al. 2013).

Our goal is to examine a key outcrop section of the Králíky-Śnieżnik antiform where the continental subduction fabrics are almost completely transposed during simultaneous horizontal shortening and vertical melt transfer. On this key section, rock types range from augen to banded orthogneiss, to schlieren and nebulitic migmatites. These rocks are studied using microstructural qualitative analysis, whole-rock geochemistry and quantitative petrological modelling to illustrate open-system behaviour where melt percolates through granitic protolith during homogeneous crustal-scale deformation. By means of thermodynamic modelling it will be shown, that homogeneous pervasive melt percolation associated with grain-scale deformation contributes to the exhumation of partially molten crust en masse. We discuss homogeneous deformation of crust, mineral transformations of solid phases and the mutual interactions of melt with the rocks during syn-deformational melt percolation. Furthermore, we argue that pervasive melt percolation is the principal mechanism controlling exhumation of deep continental crust in hot collisional orogens of which the Bohemian Massif is a world example.

GEOLOGICAL SETTING

The OSD is considered to be a part of the high-grade Moldanubian–Lugian zone representing deeply eroded Variscan orogenic root (Fig. 1a; e.g. Franke and Zelazniewicz, 2000; Aleksandrowski and Mazur, 2002). The structure of the OSD corresponds to a mantled gneiss dome with a core formed by medium- to high-grade metamorphic rocks surrounded by low-grade slates and meta-volcanics (Fig. 1b; e.g. Don et al. 1990; Mazur and Aleksandrowski, 2001). The central part of the dome is made up by antiforms cored by felsic orthogneiss with eclogite and H*P* granulite lenses (Kozłowski, 1961; Smulikowski, 1967; Pouba et al. 1985), alternating with N-S trending synforms formed mainly by metasedimentary sequences (Fig. 1b). The felsic orthogneiss types are traditionally divided into coarse-grained augen to banded Śnieżnik and fine-grained mylonitic to migmatitic Gierałtów orthogneiss (e.g. Fischer, 1936;

Lange et al. 2002; Żelaźniewicz et al. 2002; Chopin et al. 2012b). The orthogneiss protolith corresponds to a granite emplaced at *c*. 510–490 Ma within a host metasedimentary sequence (e.g. Oliver et al. 1993; Borkowska and Dörr, 1998; Kröner et al. 2000; 2001; Lange et al. 2005; Bröcker et al. 2009; Mazur et al. 2010). The protolith age of the (U)H*P* granulite facies rocks remains still controversial but it is probably older than *c*. 470 Ma (Štípská et al. 2004; Lange et al. 2005; Anczkiewicz et al. 2007; Bröcker et al. 2009; Bröcker et al. 2010). The metasedimentary sequences (Mlynowiec and Stronie formations) are dominated by Neoproterozoic to Cambro-Ordovician paragneiss and micaschist sporadically interbedded with layers of varied lithologies, such as metavolcanic rocks and few lenses of quartzite, graphite schist and marble (Don et al. 1990, 2003).

The metasediments and orthogneiss together with (U)H*P* rocks were affected by an Early Carboniferous metamorphism (*c*. 340 Ma; e.g. Turniak et al. 2000; Štípská et al. 2004; Lange et al. 2005; Anczkiewicz et al. 2007; Bröcker et al. 2009; Jastrzębski, 2009; Bröcker et al. 2010). The orthogneiss shows amphibolite- to eclogite-facies conditions with peak estimates ranging from ~20 kbar/700 °C to ~27 kbar/700–800 °C (e.g. Bakun-Czubarow, 1992; Bröcker and Klemd, 1996; Klemd and Bröcker, 1999; Štípská et al. 2004; Chopin et al. 2012b), whereas the metapelites preserve an amphibolite-facies metamorphism reaching *P*–*T* conditions of ~5–9 kbar and ~460–650 °C (Murtezi, 2006; Jastrzębski, 2009; Jastrzębski et al. 2010; Skrzypek et al. 2011a,b; Štípská et al. 2012; Skrzypek et al. 2014;). UH*P* metamorphism (reaching ~30 kbar) was proposed for eclogite and H*P*-granulite (Bakun-Czubarow, 1991, 1992; Kryza et al. 1996; Klemd and Bröcker, 1999; Ferrero et al. 2015; Jedlička et al. 2017), while other authors suggest lower *P*–*T* conditions of ~19–22 kbar at 700–800 °C for the eclogite (Bröcker and Klemd, 1996; Štípská et al. 2012) and ~18–22 kbar at 800–1000 °C for the granulite (Pouba et al. 1985; Steltenpohl et al. 1993; Štípská et al. 2004; Bröcker et al. 2010; Budzyń et al. 2015). Retrograde metamorphism has been estimated

at ~4–9 kbar and 550–700 °C for the eclogite (Klemd et al. 1995; Bröcker and Klemd, 1996; Štípská et al. 2012), and at ~8–12 kbar and 560–800 °C for the granulite (Steltenpohl et al. 1993; Štípská et al. 2004). Numerous cooling ages at *c*. 350–330 Ma were obtained using Rb–Sr and ^{40}Ar–^{39}Ar phengite and biotite dating (e.g. Steltenpohl et al. 1993; Maluski et al. 1995; Białek and Werner, 2004; Lange et al. 2005; Schneider et al. 2006; Anczkiewicz et al. 2007; Bröcker et al. 2009; Chopin et al. 2012a).

Available geological, geochronological and geophysical data allowed to divide the tectonic evolution of the OSD into three main stages: (1) H*P* metamorphism of Late Devonian – Early Carboniferous age associated with continental underthrusting of the Saxothuringian crust beneath the autochthonous Teplá-Barrandian type Neoproterozoic crust (Fig. 1a, b; Chopin et al. 2012b; Mazur et al. 2012). (2) Extrusion of a Saxothuringian-derived high-grade metamorphic core through the upper crust of the upper plate in front of the Brunia microcontinent. This event is responsible for exhumation of H*P* rocks and their re-equilibration at mid-crustal conditions (Štípská et al. 2004; 2012), while metasediments were simultaneously buried in marginal synforms (Skrzypek et al. 2011a,b, 2014; Štípská et al. 2012). (3) Ductile thinning event associated with formation of detachments and unroofing of the apical part of the dome (Pressler et al. 2007; Chopin et al. 2012a; Lehmann et al. 2013).

The south-eastern part of the OSD

The south-eastern part of the OSD represents a type section through the extruded Saxothuringian-derived crustal portion, where structural and petrological evolution of rocks affected by vertical ductile flow can be studied (see Fig. 1b). This section consists of the gneissic Międzygórze antiform in the west and the Králíky-Śnieżnik antiform in the east, separated from each other by a metasedimentary synform cropping out mainly in the Morava valley (Figs. 1c and 2a; Don, 1964, 1982; Chopin et al. 2012a; Štípská et al. 2012).

The previously well studied Międzygórze antiform is formed by an orthogneiss cored by a N-S trending belt of eclogite lenses (Figs. 1c and 2a; Chopin et al. 2012a,b; Štípská et al. 2012). Here, low-strain augen orthogneiss was progressively transformed into a banded to migmatitic orthogneiss (Chopin et al. 2012b). The banded and migmatitic orthogneiss are the most abundant in a ~1.5 km wide zone around the eclogite belt, whereas the augen orthogneiss is developed east of the high-grade orthogneiss-eclogite core (see Fig. 2a). The distinct textural varieties of the three orthogneiss types were interpreted as a result of deformation and metamorphism of the same Cambrian granite protolith, reflecting mostly strain gradient and migmatization (Turniak et al. 2000; Lange et al. 2005; Chopin et al. 2012b), but also variable degree of melt-rock interaction (Štípská et al. 2019).

In the Międzygórze antiform, the augen orthogneiss displays a sub-horizontal S1 foliation (Fig. 2a), which is deformed by asymmetrical m- to km-scale open upright F2 folds associated with progressive transposition into a N-S striking subvertical S2 metamorphic foliation in the banded to migmatitic orthogneiss (Chopin et al. 2012a,b; Štípská et al. 2012; 2019). Finally, the S2 migmatitic foliation was heterogeneously reworked by a weakly developed F3 recumbent folds and rare sub-horizontal S3 axial plane cleavage (Fig. 2a). The banded to migmatitic orthogneiss adjacent to the eclogite experienced prograde evolution along a H*P* gradient reaching eclogite-facies conditions similar to that of the adjacent eclogite. This implies that both lithologies shared the same process of burial to ~19–20 kbar and >700 °C (Chopin et al. 2012b; Štípská et al. 2012). This contrasts with the conditions from augen orthogneiss in direct continuity with paragneiss in the synforms, which show maximum burial conditions of ~7.5–8.0 kbar and ~600–620 °C (Jastrzebski et al. 2017). Recent mineral equilibria modelling of Štípská et al. (2019) reveals that the migmatitic orthogneiss types were equilibrated at ~15–17 kbar and ~690–740 °C during infiltration of a granitic melt. Retrograde equilibration down to ~7−10 kbar was largely restricted to retrograde zoning in

phengite, garnet and plagioclase, and crystallization of biotite around phengite and garnet. Here, Early Carboniferous metamorphic ages of *c.* 340–360 Ma were determined on zircon rims in migmatitic orthogneiss (Turniak et al. 2000; Lange et al. 2005) and on zircon in leucosomes and leucocratic veins (Bröcker et al. 2009).

In the Morava valley metasedimentary synform, microstructural evidence suggests that the S1 fabric is associated with prograde metamorphism along a M*P*–M*T* gradient reaching garnet- to staurolite-grade conditions at ~6 kbar/580 °C (Štípská et al. 2012). A continuous growth of both garnet and staurolite parallel to S2 indicates prograde metamorphism up to ~7.5 kbar/630 °C in the sub-vertical fabric. However, chlorite parallel to the S2 foliation suggests that retrograde metamorphism and exhumation to ~5 kbar/500 °C also occurred during this deformation event. The *P*–*T* path related to D3 was a prolonged retrograde evolution towards temperature lower than 550 °C (Štípská et al. 2012).

In the eastern N-S trending Králíky-Śnieżnik antiform, the augen to banded mylonitic orthogneiss is rare and the bulk of the antiform is formed by a migmatitic orthogneiss. Eclogites lenses occur in places in the migmatitic orthogneiss and in the north the core of the antiform is formed by intermediate to felsic H*P* granulites (Fig. 1c; Pouba et al. 1985; Štípská et al. 2004). The whole Králíky-Śnieżnik antiform is characterized by significantly higher degree of migmatization compared to the westerly Międzygórze antiform (Figs. 1c and 2b). Recent petrological studies from the granulite belt indicate UH*P* conditions of ~20–25 kbar and ~550–950 °C (Budzyń et al. 2015; Jedlička et al. 2017) which is consistent with melt inclusion study from felsic granulites that show trapping conditions for melt at ~27 kbar and ~875 °C, suggesting near UH*P* conditions of melting (Ferrero et al. 2015). The age of metamorphism is constrained by U–Pb dating of zircon to ~340 Ma (Štípská et al. 2004).

In the Králíky-Śnieżnik antiform, the rare relics of the earliest S1 fabric are systematically related to various types of migmatitic orthogneiss. These structures are mostly transposed by the dominant N-S sub-vertical S2 foliation (Fig. 2b). The whole domain is characterized by decimetre-scale transitions from remnants of partially molten porphyritic 'augen' to 'banded' orthogneiss and finally, to 'fine-grained' migmatitic orthogneiss (Figs. 1c and 2b; Don, 1982; Chopin et al. 2012a). This type of transition is classically referred as the so-called Śnieżnik augen gneiss – Gierałtów gneiss transition in the whole OSD (Lange et al. 2002 and references therein). However, this distinction is descriptive and only rarely took into account the processes leading to the gradual development of these rock types (Chopin et al. 2012a,b; Štípská et al. 2012).

FIELD RELATIONS AND STRUCTURAL EVOLUTION

Field relations and textural types of the orthogneiss were examined along a representative outcrop in the central part of the Králíky-Śnieżnik antiform (UTM WGS84 coordinates X=632590 and Y= 5550699; Figs. 1c and 2b). Here, the textural types of orthogneiss (see Fig. 3) range from augen to banded orthogneiss (samples FC076A, B and E) and fine-grained migmatitic orthogneiss (samples FC076C, D, F, I and J). Relics of S1 foliation preserved in the augen and banded orthogneiss are folded by cm- to dm-scale upright close to isoclinal F2 folds (Fig. 3, samples FC076A-B and E). However, in the fine-grained migmatitic rocks the S1 foliation is completely overprinted by a N-S striking subvertical S2 fabric (Fig. 3, samples FC076D and C) that reflects important E-W shortening (Fig. 3, sample FC076E). The internal structure of the syn-anatectic S2 foliation in the migmatite is defined by the orientation of polymineral layers with weakly oriented micas, and locally by elongated relict domains of schlieren or "ghosts" of felsic patches (see white arrow in Fig. 3). In addition, the textural transition from augen to banded and migmatitic orthogneiss is commonly gradational and perpendicular to the S2 foliation (Fig. 3; see sample FC076I). Therefore, this textural trend

may indicate not only deformation gradient but also variable proportion of melt fraction (see Závada et al. 2018).

MICROSTRUCTURAL AND PETROGRAPHIC FEATURES

Microstructural and petrological studies were carried out on 10 samples collected along the outcrop section (see Fig. 3 for localization of samples). Characterization of the different orthogneiss types was carried out by combining optical microscopy and back-scattered electron imaging (BSE) on XZ oriented thin sections. BSE images were acquired by a Tescan VEGA\\XMU electron microscope at the EOST laboratory of the University of Strasbourg (France) and at the Charles University in Prague (Czech Republic). Microstructural and petrographic features are documented in Figures 4 and 5.

In all the rock types, the mineral assemblage is plagioclase, K-feldspar, quartz, white mica, biotite and garnet. Apatite and zircon are present as accessory minerals in the matrix, ilmenite is only enclosed in biotite. Mineral abbreviations used here are: ksp, K-feldspar; pl, plagioclase; q, quartz; bi, biotite; g, garnet; ap, apatite; ilm, ilmenite; myr, myrmekite (mainly after Holland and Powell, 1998). In addition, the mineral abbreviation of white mica (wm) is used in diagrams because the composition of white mica ranges from phengite (ph) to muscovite (mu), whereas phengite is used where the observed white mica has phengitic composition.

In the following microstructural descriptions, we use the orthogneiss classification of Štípská et al. (2019) which is based on different distribution of K-feldspar, plagioclase and quartz that ranges from monomineral recrystallized layers to isotropic distribution, and also involves different amount and distribution of interstitial phases (Fig. 4). These authors defined three textural types related to variable degree of melt-rock interaction: banded type I – mylonitic augen and banded orthogneiss with sharp boundaries between monomineral aggregates; banded type II – augen and banded orthogneiss with diffuse boundaries between

monomineral aggregates; and schlieren and nebulitic migmatites. In the studied area the augen to banded type I orthogneiss has not been recognized. Common variety is the augen to banded type II orthogneiss composed of monomineral layers of recrystallized K-feldspar (2 to 10 mm thick) with interstitial phases. These layers are alternating with monomineral layers of plagioclase and quartz (1 to 4 mm thick) parallel to the S1 in F2 fold limbs and/or to the axial planar S2 foliation and have always diffuse boundaries between individual layers that are interlobed with adjacent minerals (Fig. 4, sample FC076B). The banded type II orthogneiss shows 1 to 4 mm thick layers of K-feldspar, plagioclase and quartz-rich domains with increasing proportion of interstitial phases in K-feldspar aggregates. Characteristic feature is gradational diffuse and poorly defined boundaries between originally monomineral layers (Fig. 4, sample FC076E). This variety can be considered as a more advanced stage of disintegration of originally monomineral aggregates. For fine-grained migmatitic rocks we use the term schlieren migmatite for an almost isotropic migmatite with small K-feldspar-rich domains elongated parallel to S2 foliation within a matrix characterized by random distribution of phases (Fig. 4, sample FC076J); and the term nebulitic migmatite for an isotropic migmatite characterized by random distribution of all the phases (Fig. 4, sample FC076C). In Figure 4, the studied rock types are organized in sequence characterized by gradual disappearance of original monomineral layering.

K-feldspar-rich layers

The K-feldspar-rich layers occur mainly in the augen-banded type II and banded type II orthogneiss and are preserved in schlieren migmatites (Fig. 4). K-feldspar almost monomineral aggregates are slightly elongated and composed of irregular grains of 50–1000 μm in size (Fig. 5a). Large grains of K-feldspar show a well-developed shape preferred orientation parallel to the macroscopic foliation, whereas preferred orientation of smaller grains is less developed (Fig. 5a). The boundaries between elongated K-feldspar grains are

serrated and lined by irregular <10–30 µm wide films of plagioclase, irregular plagioclase crystals 10−300 µm in size and by rounded quartz 10−500 µm in size. K-feldspar grains show cuspate-lobate boundaries with respect to interstitial plagioclase and quartz (Fig. 5b). Small myrmekite-like aggregates 10−200 µm in size are also present along the K-feldspar grains within the K-feldspar-rich layers (Fig. 5b). Myrmekite is composed mostly of fine-grained plagioclase and quartz, with small and rare grains of K-feldspar and white mica. The proportion of interstitial quartz, plagioclase and myrmekite in the K-feldspar-rich domains is increasing from the augen-banded type II to schlieren migmatite (see Fig. 4).

Plagioclase- and quartz-rich layers

The plagioclase- and quartz-rich layers occur only in the augen-banded type II and banded type II orthogneiss. Plagioclase aggregates are made of equigranular grains 50–800 µm in size that form a granoblastic microstructure. The plagioclase grains do not display a visible shape preferred orientation (Fig. 5c). The rounded and isolated quartz (10−100 µm) and cuspate small K-feldspar (10−50 µm in size) occur as interstitial grains at triple junctions of the plagioclase grains. Boundaries between plagioclase grains are mostly irregular and the presence of numerous cuspate K-feldspar and isolated rounded quartz grains in the plagioclase-rich layers increases from the augen-banded type II to banded type II (Fig. 4). In addition, layers rich in polygonal plagioclase (1500−2500 µm) with antiperthite core are locally observed parallel to the S2 foliation (Figs. 4 and 5d).

Quartz forms completely recrystallized aggregates composed of large and inequigranular grains 30−2000 µm in size with amoeboid to highly lobate boundaries (Fig. 4). They show a weak shape preferred orientation. Feldspar crystals penetrate heterogeneously into quartz aggregates along mutually lobate boundaries (Fig. 5c).

Numerous grains of white mica, biotite, garnet and accessory minerals occur within the layers dominated by plagioclase and quartz (Figs. 4 and 5c). White mica forms commonly

large laths (250–1000 μm in size) with small or large biotite at its margins, along its cleavage or in its crystallographic continuity (Fig. 5e). These features indicate that biotite grew at the expense of white mica, as was proposed by Štípská et al. (2019). Both white mica and biotite are strongly oriented parallel to the monomineral layers observed in the banded type II. The proportion of white mica is higher compared to biotite (around 70% and 30% of all micas respectively). However, the amount of biotite increases from the augen-banded type II to nebulitic migmatite reaching >40% of the total amount of the micas (Fig. 4). Biotite is partially or completely chloritized. Garnet (<2 vol. %) has irregular shapes and is commonly fragmented (Fig. 5f). Normally, it occurs as small relict grains (around 50–200 μm) inside plagioclase or quartz, or as small (up to 500 μm) grains at contact with plagioclase and quartz, but in some places it is also in contact with white mica and biotite.

Polymineral layers

Polymineral layers occur in all studied rock varieties and are characterized by a mixture of fine-grained phases, described as mixed aggregates in Figure 4. In the mixed aggregates, K-feldspar, plagioclase and quartz grains are highly irregular and surrounded by abundant myrmekite and small interstitial phases. White mica, biotite and garnet are dispersed in aggregates of K-feldspar, plagioclase and quartz (Fig. 5f), and white mica and biotite are strongly to weakly oriented parallel to the S2 foliation. Locally, K-feldspar is replaced at its rim by quartz-white mica symplectite when it occurs at contact with white mica (Fig. 5g).

As interpreted by Štípská et al. (2019), transition from the augen-banded type II to nebulitic migmatite is caused by increasing nucleation of interstitial phases along like-like grain boundaries and by progressive disintegration of recrystallized feldspar grains by embayment of fine-grained myrmekite (Fig. 4).

MINERAL CHEMISTRY

Samples corresponding to different orthogneiss types were selected for mineral chemical analysis. Minerals were analysed using the *Electron Probe Micro-Analyser* (EPMA) JEOL 8200 at the University of Lausanne (Switzerland) and Jeol FEG-EPMA JXA-8530F at the Charles University in Prague (Czech Republic). The analyses were made in point beam mode at 15-kV acceleration voltage and 20-nA beam current, with a spot diameter of 5 μm and a counting time of 20–30 s. Representative analyses of feldspar, micas and garnet are presented in Tables 1, 2 and 3 and shown in Figures 6–9. Abbreviations used for mineral end-members in molar proportions are an = Ca/(Ca+Na+K); ab = (Na/(Ca+Na+K); or = K/(Ca+Na+K); X_{Fe} (ph, bi, g) = $Fe_{total}/(Fe_{total} + Mg)$; alm = $Fe^{+2}/(Fe^{+2} + Mg + Ca + Mn)$; sps = $Mn/(Fe^{+2} + Mg + Ca + Mn)$; grs = $Ca/(Fe^{+2} + Mg + Ca + Mn)$ and prp = $Mg/(Fe^{+2} + Mg + Ca + Mn)$. The sign "→" indicates a trend in mineral composition or zoning, the sign "–" depicts a range of mineral compositions and p.f.u. is per formula unit.

Feldspar

Recrystallized K-feldspar has subtle zoning within all the orthogneiss types (Fig. 6a–f, Table 1), whit cores more albite-rich (or = 0.86–0.90) compared to rims (or = 0.90–0.94). K-feldspar in small grains in myrmekite (Fig. 6a–c), and K-feldspar forming thin films or small interstitial grains in the layers dominated by plagioclase and quartz has a lower content of albite (or = 0.92–0.96) (Fig. 6a, b).

Two distinct plagioclase populations have been measured according to their microstructural position (Fig. 6a–f, Table 1). Plagioclase aggregates exhibit homogeneous oligoclase composition (an = 0.12–0.22), whereas more sodic composition (an = 0.02–0.05) is found in small interstitial plagioclase grains and thin films coating the K-feldspar aggregates of the augen-banded type II, banded type II and schlieren migmatite (Fig. 6a). Albite (an = 0.02–0.09) is also found in myrmekite-like aggregates within all the rock types (Fig. 6e, f).

Micas

White mica shows in all rock types zoning from core to rim, with decreasing Si from ~3.20−3.40 p.f.u. to ~3.10−3.20 p.f.u., Ti from ~0.08−0.03 p.f.u. to ~0.01−0.03 p.f.u. and with increasing $X_{Fe(tot)}$ from ~0.50−0.55 to > 0.55 (Fig. 7a–d, Table 2). F content varies from 0.04 to 0.14 p.f.u. with higher values in the core (Fig. 7c, Table 2).

Biotite has similar compositional ranges in all the rock types: in augen-banded type II, Ti = 0.05–0.15 p.f.u., Al = 1.70–1.95 p.f.u., X_{Fe} = 0.74–0.78 and F = 0.20–0.25 p.f.u.; in banded type II, Ti = 0.10–0.20 p.f.u., Al = 1.65–1.75 p.f.u., X_{Fe} = 0.74–0.78 and F = 0.10–0.25 p.f.u; in schlieren migmatite, Ti = 0.05–0.12 p.f.u., Al = 1.75–1.90 p.f.u., X_{Fe} = 0.75–0.78 and F = 0.10–0.20 p.f.u.; and in nebulitic migmatite, Ti = 0.12–0.20 p.f.u., Al = 1.65–1.75 p.f.u., X_{Fe} = 0.76–0.78 and F = 0.10–0.20 p.f.u. (Fig. 8, Table 2).

Garnet

Garnet exhibits a flat or significant compositional zoning in samples of augen-banded type II to schlieren migmatite (Fig. 9a–c, Table 3), whereas in samples of the nebulitic migmatite garnet displays a strong zoning (Fig. 9d, Table 3). In augen-banded type II to schlieren migmatite, some garnet shows flat profiles with high X_{Fe} (0.95–0.98) and almandine ($alm_{0.65–0.72}$), low pyrope ($prp_{0.02–0.04}$), grossular ($grs_{0.07–0.09}$) and spessartine ($sps_{0.10–0.19}$) (Fig. 9a–c, Table 3). In some garnets of the augen-banded type II to schlieren migmatite, grossular decreases ($grs_{0.18→0.09}$) and spessartine increases ($sps_{0.09→0.19}$) from core to rim (Fig. 9a–c, Table 3). In the nebulitic migmatite, garnet has higher grossular and lower spessartine in the core compared to augen-banded type II, banded type II and schlieren migmatite, and garnet zoning is from core to rim marked by decrease in grossular ($grs_{0.34→0.09}$) and increase in almandine ($alm_{0.59→0.68}$) and spessartine ($sps_{0.04→0.21}$), and accompanied by a flat trend in high X_{Fe} (0.95–0.98) and low pyrope ($prp_{0.02–0.04}$) (Fig. 9d, Table 3).

WHOLE-ROCK CHEMISTRY

Whole-rock major- and trace-element analyses were performed by *Inductively Coupled Plasma-Atomic Emission Spectroscopy* (ICP-AES) and -*Mass Spectrometry* (ICP-MS) at the Acme laboratories of Canada for each rock type. Analyses are summarized in Table 4 and presented in a series of isocon diagram (Fig. 10a; Grant, 1986) and spider plots (Fig. 10b, c) to show geochemical variations. The isocon diagram in Fig. 10a points to a similar composition of major elements for all the studied rock types, suggesting negligible losses and gains of major elements during the process of deformation and partial melting. The negligible losses and gains of major elements suppose that there were no variations in volume (Marquer and Burkhard, 1992). In other words, the major element analyses suggest that they all the rock types originated from the same protolith.

The comparison of trace-element concentrations among individual samples and compared to different rock groups described by Chopin et al. (2012b) are done in spider plots normalized to Chondrite (Evensen et al. 1978, Fig. 10b). According to Chopin et al. (2012b), the LREE (La, Ce, Pr and Nd) and MREE (Sm, Eu and Gd) contents drop slightly in the sequence from augen to banded and migmatitic orthogneiss, whereas the HREE distribution is homogenous (see shaded fields in Fig. 10b). However, the character of distribution patterns for all studied samples is fairly homogeneous, showing similar REE contents (spanning ΣREE = 55–89 ppm., Table 4) and subparallel distributions. Consequently, significant differences between the rock types are not recognized; although, generally subparallel patterns loosely vary in LREE and MREE, where the nebulitic migmatite (sample FC076C) is slightly depleted in comparison with the augen-banded type II, banded type II and schlieren migmatite. In addition, the compositional ranges overlap the migmatitic group described by Chopin et al. (2012b), showing stronger depletion in the magnitude of their negative Eu anomalies (Fig. 10b). This fact indicates that the studied samples are comparable to the end-

394 members characterized by presence of interstitial melt from the rock sequence described by
395 Chopin et al. (2012b).

396 In Figure 10c, a compositional variation between the different rock types is presented in
397 the spider plot normalized by an augen-banded type II (sample FC076A), where the character
398 of distribution patterns for all studied samples shows essentially similar composition with the
399 exception of As, Pb and Ni. Therefore, the overall resemblance in the trace-element
400 distribution patterns and only gradual changes in the elemental concentrations argue against
401 significant differences in the protolith.

402 To constrain better the relative mobility of melt and/or fluids among the rock types, mass
403 balance calculations on incompatible elements among the augen-banded type II (sample
404 FC076A) and the banded type II (sample FC076E) and the different fine-grained migmatites
405 have been performed using the normalized Potdevin diagram (Figure 11 and Table 5;
406 Potdevin and Marquer, 1987; Lopez-Moro, 2012). In Figure 11, the behaviour of each
407 element is represented by a straight line. The black thick-line corresponds to the chemical
408 composition of the augen-banded type II. Mass balance calculation shows a slight gain with
409 respect to augen-banded type II in a range of incompatible elements, such as HREE, Ba, Sr,
410 Eu, K and Rb in all the rock types. The gain in Ba, Sr, Eu, K and Rb, together with the
411 presence of marked negative Eu anomalies in Figure 10b, seems to bear a testimony to a
412 heterogeneous nucleation of interstitial feldspar from percolated melt (e.g. Hasalová et al.
413 2008; Goncalves et al. 2012; Závada et al. 2018). In the banded type II and schlieren
414 migmatite, the LREE and MREE elements show gains while U, Zr, Cs, Nb, Hf and Ta
415 elements show loss. These compositional ranges in the banded type II and schlieren migmatite
416 suggest that REE-bearing minerals such as monazite (containing LREE and Th) and apatite
417 (containing MREE) crystallized while zircon (containing Zr) was removed by the melt.
418 However, the nebulitic migmatite shows a depletion of LREE, MREE and Th, reflecting the

dissolution of monazite and apatite in the melt. Therefore, this change can be considered as a result of melt infiltration/percolation of granitic sources under open-system conditions (e.g. Hasalová et al. 2008; Goncalves et al. 2012; Závada et al. 2018).

FORWARD MODELLING OF MIGMATITIC ORTHOGNEISS

In the modelling of anatexis of granitic rocks at eclogite-facies conditions we follow the approach discussed in Štípská et al. (2019). We model the assemblages metastable with respect to the stability of clinopyroxene, as clinopyroxene is commonly absent in quartzo-feldspathic rocks with (U)H*P* conditions (e.g. Young and Kylander-Clark, 2015). We use the haplogranitic melt model even if it was not calibrated specifically for high-pressure conditions, as it was shown that modelling with this melt model is able to explain well mineral equilibria in quartzo-feldspathic rocks at H*P*–H*T* conditions (Štípská et al. 2008; Hopkins et al. 2010; Lexa et al. 2011; Nahodilová et al. 2014).

Pseudosections were calculated using THERMOCALC 3.33 (Powell et al. 1998; version 2009) and dataset 5.5 (Holland and Powell, 1998; January 2006 upgrade), in the system MnO-Na_2O-CaO-K_2O-FeO-MgO-Al_2O_3-SiO_2-H_2O-TiO_2-O (MnNCKFMASHTO). The activity-composition relationships used are as follows: for silicate melt (liq), from White et al. (2007); for garnet (g), biotite (bi) and ilmenite (ilm), from White et al. (2005); for feldspar (pl, ksp), from Holland and Powell (2003); for white mica (wm), from Coggon and Holland (2002); and, for cordierite (cd), from Holland and Powell (1998). The calculations are done for the whole-rock composition of a nebulitic migmatite (sample FC076C; Table 4). Because of closely similar whole-rock compositions of the other samples (Fig. 10a) the calculated diagrams are also used for interpretation of their metamorphic evolution. The amount of H_2O in the whole-rock composition was deduced from *T*–*M*(H_2O) pseudosection (see description below, Fig. 12). Mineral composition isopleths of garnet, white mica, plagioclase and molar proportion of liquid were plotted to discuss *P*–*T* conditions of mineral equilibration. The

isopleth notation used is: m(sps) = Mn/(Ca+Mg+Fe+Mn)*100; x(alm) = Fe/(Ca+Mg+Fe+Mn)*100; z(grs) = Ca/(Ca+Mg+Fe+Mn)*100; Si(wm) p.f.u.; ca(pl) = Ca/(Ca+Na+K) and liq (mol. %).

T–M(H_2O) pseudosection at 7 kbar

In order to estimate the conditions of last equilibration in migmatites, it is assumed that the assemblage tends to equilibrate until it becomes melt poor or melt absent near or at the solidus (e.g. Štípská and Powell, 2005; Hasalová et al. 2008c). Therefore, a T–M(H_2O) pseudosection at a pressure of 7 kbar was calculated first, simulating conditions of last equilibration with melt near the solidus (Fig. 12). The observed assemblage of q-pl-ksp-g-bi-wm-ilm-liq is stable at T–M(H_2O) = ~0.30–0.53 and at ~630–710 °C and the observed garnet rim composition (~alm_{68}; grs_{10}; sps_{20}) fits the calculated isopleths at conditions of T–M(H_2O) = ~0.52 and ~630 °C (Fig. 12). Therefore, it is assumed that the rocks crossed the solidus with minimum H_2O content corresponding to 2.07 mol. % of H_2O in the whole-rock composition.

Closed-system P–T pseudosection

The P–T diagram was calculated for an amount of H_2O = 2.07 mol. % deduced from the T–M(H_2O) diagram (see Fig. 12 and related discussion). This H_2O amount allows also the stability of H_2O-free and garnet-free assemblage (~5.2–6.7 kbar and <550–620 °C), typical of a granite at MP–MT conditions and therefore may illustrate rock evolution in a closed system, even for H_2O. The major features and topology of the diagram involve a H_2O-saturated solidus up to ~7.8 kbar followed by a steeply inclined H_2O-undersaturated solidus from ~7.8 kbar to higher pressure at progressively higher temperature. The biotite-out and garnet-out lines are temperature sensitive at suprasolidus and subsolidus conditions, respectively and pressure sensitive at subsolidus conditions (Fig. 13).

The resulting P–T phase diagram shows a stability field of q-pl-ksp-g-bi-wm-ilm-liq between ~4–12 kbar and ~630–740 °C, corresponding to the observed assemblage in all the

rock types. The mineral compositions measured in the different rock types point to last equilibration in the middle-*P* part of the q-pl-ksp-g-bi-wm-ilm-liq stability field, at ~6 kbar and ~640 °C (ellipse 2 in Fig. 13a). The nebulitic migmatite preserves high grossular content of garnet in the core (alm_{60-65}; $grs_{30–34}$; sps_4; Fig. 9d), pointing to a *P*–*T* peak in the melt-free stability field of q-pl-ksp-g-bi-wm-ru at ~14–16 kbar and ~600–740 °C (ellipse 1 in Fig. 13a−b). The high Si content in white mica in all the rock types (Si = 3.35–3.40 p.f.u.; Fig. 7a) supports these peak *P*–*T* conditions (Fig. 13c). The presence of interstitial plagioclase, quartz and K-feldspar as well as presence of myrmekite are interpreted as presence of melt at grain boundaries, causing dissolution and precipitation under the presence of melt. The plagioclase measured from these films and myrmekite shows albite composition ($an_{0.05-0.02}$), supporting crossing of the H_2O-undersaturated conditions and beginning of partial melting at ~16 kbar (Fig. 13d). The calculated isopleths of melt mode suggest a very small melt production around 1 mol. % (Fig. 13e). This calculated volume of melt suggests that the melt was isolated in melt films, pools or pockets compatible with the microstructure observation (see Fig. 5b). The absence of rutile and the core-to-rim zoning trends of garnet and white mica in the nebulitic migmatite suggest a *P*−*T* path from ~14−16 kbar and ~600–740 °C to ~6 kbar and ~640 °C, with local equilibration down to the ilmenite stability field and close to the solidus.

Additionally, the core composition of garnet in samples of augen-banded type II, banded type II and schlieren migmatite is partially to completely re-equilibrated at ~6 kbar and ~640 °C (see Fig. 9a–c), suggesting that the mineral assemblage of these rocks were melt-bearing close to the solidus. To explore consequences of a possible melt gain in the rocks, a P–X_{melt} diagram was calculated.

P–X_{melt} pseudosection for discussion of open-system melt infiltration

This P–X_{melt} pseudosection illustrates the effect of melt infiltration within an open system (Fig. 14). It was calculated at conditions of the estimated peak metamorphism (T = 700 °C),

and for a range of compositions between the H_2O-undersaturated whole-rock composition of the nebulitic migmatite (X_{melt} = 0) and the composition of the nebulitic migmatite with 20 mol. % of melt added (X_{melt} = 1; Fig. 14). Supposing that melt can be lost from the rocks undergoing melting deeper in the crust, melt composition is taken from a calculation at 16 kbar and 730 °C (see black star in Fig. 13a). The major features of the diagram involve a liquid-in line running from 12 kbar for X_{melt} = 0 to 20 kbar for X_{melt} = 0.25. The stability of biotite, rutile and ilmenite depends on pressure in the melt-absent fields and on X_{melt} in the melt-present fields. The compositional isopleths of garnet and Si-in-phengite are mainly pressure sensitive in the melt-present fields, and do not depend on the amount of melt (Fig. 14). The horizontal arrow illustrates the addition of melt to a rock with original H_2O content inferred for the protolith (Fig. 13a).

Melt percolation is considered in a prograde assemblage at 16 kbar, compatible with observed assemblage, high grossular content of garnet and high Si content of white mica. Along the horizontal arrow at 16 kbar in Figure 14, the assemblage will evolve from melt-free to melt-present stability field, while garnet and white mica compositions do not change (Fig. 14). Because the mineral compositional isopleths are not sensitive to the amount of melt added, the melt amount that was percolated is unknown.

The absence of rutile and the core-to-rim zoning trends of garnet ($alm_{60\rightarrow70}$; $grs_{34\rightarrow5}$, $sps_{4\rightarrow22}$; Fig. 9d) and white mica (Si = 3.40–3.10 p.f.u.; Fig. 7a) are compatible with a decompression path for a rock with added melt from rutile-bearing stability field at 16 kbar to ilmenite-bearing stability field at ~8−13 kbar. The difference in the prediction of the decompression path is the amount of melt present, for example being ~1 mol. % melt along the arrow A, from ~3.40 to ~7 mol. % along the arrow B or from ~15 to ~25 mol. % along the arrow C (Fig. 14). The consequence of different melt amount in different samples may be the difference in re-equilibration along the decompression path. We suggest that for the nebulitic

519 migmatite that preserves H*P* garnet core the amount of melt was low, for example along the
520 path A (and also for conditions shown in Fig. 13a), thus precluding complete garnet
521 reequilibration on decompression. Re-equilibration of garnet core close to the solidus
522 observed in augen-banded type II, banded type II and schlieren migmatite may be caused by
523 higher proportion of melt due to melt percolation. Therefore, a new *P–T* diagram with ~3.40
524 mol. % of re-integrated melt in the whole-composition was calculated for explaining better
525 the observed mineral assemblage and mineral compositions of the augen-banded type II,
526 banded type II and schlieren migmatite (see Fig. 15).

527 ***P–T* pseudosection with added melt**

528 The resulting whole-rock composition after the re-integration of 3.40 mol. % melt is
529 presented in mole percent normalized to 100% (Fig. 15a). The major features and topology of
530 the diagram involve a shift of the H_2O-undersaturated solidus to higher pressure, whereas the
531 other features and topology are similar to the H_2O-undersaturated diagram (see Fig. 13).

532 The resulting *P–T* diagram shows a stability field of q-pl-ksp-g-bi-wm-ilm-liq between
533 ~4–13 kbar and ~610–740 °C, corresponding to the observed assemblage. The *P–T* peak
534 conditions are defined by the high grossular content measured in garnet cores ($alm_{60–65}$; $grs_{30–34}$; sps_4; Figs. 9d and 15b) preserved in nebulitic migmatite and the high Si content in phengite
535
536 cores measured in all the rock types (Si = 3.35–3.40 p.f.u.; Figs. 7a and 15c). The measured
537 albite content of plagioclase films and interstitial grains is consistent with the calculated
538 isopleth of albite at these *P–T* peak conditions ($an_{0.05-0.02}$; Fig. 15d). The last equilibration at
539 ~630–640 °C and ~6 kbar is constrained by the re-equilibrated compositions of garnet ($alm_{65–70}$; $grs_{5–10}$; $sps_{20–25}$; Fig. 15b) and white mica (Si = 3.10 p.f.u.; Fig. 15c). The calculated
540
541 isopleths of melt mode suggest a melt production during retrograde path of the order of 1 mol.
542 % resulting in up to 4 mol. % for 3.40 mol. % melt added (Fig. 15e). Therefore, the mineral
543 chemistry together with the absence of rutile record a decompression path from ~15−16 kbar

and ~650–740 °C to ~6 kbar and ~640 °C, with local equilibration down to the ilmenite stability field and close to the solidus with the presence of melt. This decompression path is compatible with the one previously described in the H_2O-undersaturated diagram (Fig. 13), and differs only in the melt amount present during the peak and retrograde evolution, suggesting that higher melt amount may result in more profound reequilibration of the assemblage close to the solidus. The melt might have been added to rocks, explaining the textures, e.g. desintegration of the monomineral banding or more profound reequilibration of garnet composition, but the rocks may also undergo variable degree of melt loss on decompression before last cooling through the solidus.

DISCUSSION AND CONCLUSIONS

The core of the Orlica-Śnieżnik Dome (Fig. 1b) consists of two antiforms affected by various degrees of migmatization related to their distance from the site of presumed continental subduction further west (see Fig. 13 in Chopin et al. 2012a). The proximal and small Międzygórze antiform (~1 km across and ~4 km long; Fig. 1c) is characterized by heterogeneously developed zones of partial melting surrounding blocks of well-preserved H*P* rocks. The distal large-scale Králíky-Śnieżnik antiform (~6–8 km across and ~20 km long) was affected by widespread melting and almost complete re-equilibration of H*P* mineral assemblages. In this work the orthogneiss and migmatite of the Králíky-Śnieżnik antiform are compared with those of the Międzygórze antiform in order to understand the role of melt-deformation interplays during the exhumation of large portions of continental crust in Variscan continental collision zone.

Microstructural and geochemical arguments for grain-scale melt percolation during D2 deformation

In the study area, relics of shallow-dipping S1 foliation are reworked by vertical F2 folds and almost pervasive N-S trending subvertical S2 foliation. This structural succession is the same as in the Międzygórze antiform but the scale and degree of fabric transposition is significantly larger reaching the width of ~6–8 km and thereby attesting to large-scale orogenic process. A well-preserved and continuous transition from augen to banded orthogneiss to schlieren and nebulitic migmatite (see Figs. 3 and 4) is documented on a representative outcrop section in the central part of the Králíky-Śnieżnik antiform (see Fig. 1c). This continuous transition between different rock types, their identical mineral assemblage as well as mineral and whole-rock compositions indicate that these rock types evolved from the same granitic protolith (see Figs. 5 to 11), as was previously suggested by Lange et al. (2005) and Chopin et al. (2012a,b) in the Międzygórze antiform. Therefore, OSD may represent a large batholith formed by different magma pulses.

Further, the continuous transition from augen to banded orthogneiss to schlieren and nebulitic migmatite is related to subvertical S2 transposition (Fig. 3). The q-pl-ksp-g-bi-wm-ilm assemblage observed in all orthogneiss and migmatite types is the same despite variations in meso- and micro-scale structural and textural features (see Figs. 3 and 4). Therefore, in analogy to the Międzygórze antiform the studied sequence of rocks can be interpreted to reflect the intensity of deformation and degree of melt-rock interaction. This process is manifested by the presence of cuspate K-feldspar in plagioclase layers, quartz and albite-rich plagioclase intergrowths in K-feldspar aggregates, amoeboid grains of K-feldspar in quartz layers and diffuse boundaries between different felsic layers (see Figs. 4 and 5). All these microstructural features are interpreted as a result of grain-scale melt percolation through the solid felsic rock in agreement with previously reported examples of Hasalová et al. (2008b), Závada et al. (2018) and Štípská et al. (2019) where grain boundaries were open at the micron scale to fluid/melt circulation (e.g. Oliot et al. 2014). Such interpretation is supported by mass

balance calculations of incompatible elements which show the depletion of LREE, MREE and Th compatible with partial dissolution of monazite, zircon and apatite in the melt, implying that some melt must have been lost or must have percolated through the rocks, and the gain in Ba, Sr, Eu, K and Rb corresponding to a heterogeneous nucleation of interstitial feldspar from percolated melt (Fig. 11).

P–T evolution and melt transfer

The *P–T* path deduced from the forward-modelling indicates that the orthogneiss underwent a decompression from *P–T* peak conditions of ~15–16 kbar and ~650–740 °C to ~6 kbar and ~640 °C, where they crossed the wet solidus (see Figs. 13 and 15). The estimated *P–T* peak conditions are recorded by the presence of Ca-rich garnet cores in the nebulitic migmatite and composition of phengite in all the rock types. Subsequent decompression to ~6 kbar is recorded by the cores-to-rims zoning trends of garnet and white mica and absence of rutile. Similar *P–T* evolutions have been repeatedly reported from other rock types such as eclogite or H*P* granulite occurring in the orthogneiss (~18–30 kbar and ~700–1000 °C; e.g. Pouba et al. 1985; Bakun-Czubarow, 1991, 1992; Steltenpohl et al. 1993; Bröcker and Klemd, 1996; Kryza et al. 1996; Klemd and Bröcker, 1999; Bröcker et al. 2010; Štípská et al. 2012; Ferrero et al. 2015; Budzyń et al. 2015; Jedlička et al. 2017) with retrograde paths ranging from ~9 kbar/~730 °C to ~6 kbar/~560 °C (Steltenpohl et al. 1993; Bröcker and Klemd, 1996; Štípská et al. 2004, 2012). Recently, prograde H*P* metamorphism was attributed to the S1 fabric in the granitic orthogneiss close to the eclogite in the Międzygórze antiform (~13−18 kbar/~700–800 °C; e.g. Chopin et al. 2012b). It was also shown that migmatization of orthogneiss surrounding the Międzygórze eclogite started in eclogite-facies conditions at ~15−17 kbar in the S1 fabric (Štípská et al. 2019). These authors also showed that the anatexis was associated with decompression along the S2 fabric from ~15−17 kbar to ~7−10 kbar/~690–740 °C. We

argue that the $P–T–d$ path, at least for the D2 vertical fabric, is comparable in both antiforms (see Fig. 16).

The modelling showed that the orthogneiss protolith from the Králíky-Śnieżnik antiform is able to produce only ~1 mol. % of melt along the $P–T$ path. However, the macro- and microstructural features are typical for advanced migmatization and attest to melt presence along grain boundaries (Figs. 4 and 5), suggesting that a higher melt proportion was present. This is possible to achieve only if H_2O is added to the rocks, but being above the conditions of the wet solidus, the hydrating fluid must have been external melt (Štípská et al. 2019). Such melt is supposed to be released by similar rocks buried deeper and this is simulated in the modelling by adding granitic melt to the whole-rock composition. The modelling did not allow estimation of the melt proportion in the rocks based on the mineral chemical composition, as the mineral chemical composition for the observed assemblage is independent on the amount of melt added (Fig. 14). However, it is supposed, that rocks that contain garnet with high grossular content characteristic for H*P* conditions contained on decompression less melt compared with rocks that show garnet with re-equilibrated grossular content (see Figs. 13–15).

The melt proportion remains unknown, and may have varied along the $P–T$ path. Melt percolation started already at ~15–16 kbar and ~650–740 °C as indicated by composition of plagioclase in myrmekite and in interstitial films, then melt equilibrated with the minerals (at least with their rim compositions) during the retrograde history to ~6 kbar and ~640 °C. However, the amount of melt percolated is not likely to be sufficient to produce a melt-supported structure required for diatexite formation (Brown, 2007; Hasalová et al. 2008), but may be sufficient to allow melt-assisted granular flow (Rosenberg and Handy, 2005). This is supported by the results of Štípská et al. (2019) from the Międzygórze antiform, where it was

shown that different migmatite textures originated from variable degree of melt-rock interaction starting at ~17 kbar and ~730 °C and ending at ~7–10 kbar.

Back-stop extrusion of partially molten crust

Grain-scale melt percolation started locally in the S1 structure as demonstrated in the Międzygórze antiform, and continued in the vertical S2 foliation where the grain-scale percolation of melt occurred along vertical narrow zones of strong deformation (Štípská et al. 2019). These zones surrounded low-strain domains preserving the shallow-dipping S1 fabric not percolated by melt or only to negligible extent (Fig. 16a). However, in the Králíky-Śnieżnik antiform the D2 deformation affects almost homogenously the whole volume of the felsic orthogneiss (Fig. 16b), implying a crustal-scale melt percolation that is also feeding granite intrusions in the upper crust (Lehmann et al. 2013). Based on our petrological data and in agreement with the results of Štípská et al. (2019) it may be concluded that melt percolation along vertical D2 deformation zones facilitated exhumation of H*P* rocks in cores of antiforms from ~60 km to ~25 km (Fig. 16), allowing the juxtaposition of these H*P* rocks with M*P* rocks that occurred in crustal-scale synforms (see also Štípská et al. 2004; Chopin et al. 2012a; Štípská et al. 2012). The above described deformation was related to horizontal shortening of collisional wedge that contributed to the vertical extrusion of partially molten crust en masse in the eastern part of the OSD. Such an extrusion of weak material is pronounced in particular close to the Brunia back-stop where massive portions of rheologically weak and partially molten rocks flowed upwards under horizontal stress from the root area of the orogenic wedge (Fig. 16). The extrusion model proposed by Thompson et al. (1997a,b) is suitable to well explain the exceptionally high rate of exhumation suggested already by Steltenpohl et al. (1993) and the shape of *P*–*T* path depicted by this study. Recently, the numerical modelling of Maierová et al. (2014) tested various parameters controlling the exhumation rates of hot gneiss domes and corresponding *P*–*T*–*t* paths such as

665 rate of convergence, heat production and erosion. These authors concluded that in the case of
666 the Orlica-Śnieżnik Dome the gravitational instability contribution was minor compared to
667 laterally forced folding leading to gneiss dome formation and exhumation of hot felsic lower
668 crust. All the above mentioned models tacitly suppose extreme weakness of thermally
669 softened hot felsic lower crust allowing homogeneous vertical flow. However, in detail both
670 meso- and micro-scale mechanism allowing the extreme drop of strength of the felsic crust
671 remain enigmatic. Only recently, natural observations from hot gneiss domes and their
672 analogue modelling suggest that partial melting can trigger detachment folding and vertical
673 flow of migmatites and granitoids (Lehmann et al. 2017). Based on our study we argue that
674 the grain-scale melt percolation (called also reactive porous flow, melt infiltration) represents
675 such a principal weakening mechanism allowing homogeneous flow of crust typical for
676 extrusion. It is probably also a principal mechanism controlling exhumation of deep partially
677 molten crust in hot collisional orogens such as the European Variscan belt.

678 **ACKNOWLEDGMENTS**

679 This work was financially supported by the Czech National Grant Agency (GAČR 16-17457S
680 and 19-25035S to P. Štípská) and the French National Agency for Research (06-1148784 to
681 K. Schulmann). We would like to thank Dr. Emilien Oliot from Montpellier University for his
682 useful discussions about fluids-rocks interactions during the course of this work. We are also
683 grateful to Dr. Martin Racek from Charles University for help with mineral chemistry
684 process.

685 **REFERENCES**

686 Aleksandrowski P, Kryza R, Mazur S, Żaba J (1997) Kinematic data on major Variscan
687 strike-slip fault and shear zones in the Polish Sudetes, northeast Bohemian Massif.
688 Geological Magazine 134(5): 727–739.

689 Aleksandrowski P, Mazur S (2002) Collage tectonics in the norhteasternmost part of the
690 Variscan Belt: the Sudetes, Bohemian Massif. In: Winchester JA, Pharaoh TC, Vernier J,
691 (eds) Palaeozoic Amalgation of Central Europe: Geological Society of London Special
692 Publications 201, pp 237–277.
693 Anczkiewicz R, Szczepański J, Mazur S, Storey C, Crowley Q, Villa IM, Thrilwall ME,
694 Jeffries TE (2007) Lu–Hf geochronology and trace element distribution in garnet:
695 Implications for uplift and exhumation of ultra-high pressure granulites in the Sudetes,
696 SW Poland. Lithos 95(3-4): 363–380.
697 Bakun-Czubarow N (1991) On the possibility of occurrence of quartz pseudomorph after
698 coesite in the eclogite-granulite rock series of the Złote Mountains in the Sudetes (SW
699 Poland). Archive Mineral 47(1): 5–16.
700 Bakun-Czubarow N (1992) Quartz pseudomorphs after coesite and quartz exsolutions in
701 eclogitic omphacites of the Złote Mountains in the Sudetes (SW Poland). Archiwum
702 Mineralogiczne 48(1-2): 3−25.
703 Białek D, Werner T (2004) Geochemistry and geochronology of the Javornik granodiorite and
704 its geodynamic significance in the Eastern Variscan Belt. Geolines 17: 22–23.
705 Borkowska M, Dörr W (1998) Some remarks on the age and mineral chemistry of orthogneiss
706 from the Ladek-Śnieżnik Metamorphic Massif – Sudetes, Poland. Terra Nostra 98(2): 27–
707 30.
708 Bröcker M, Klemd R (1996) Ultrahigh-pressure metamorphism in the Śnieżnik Mountains
709 (Sudetes, Poland): P-T constraints and geological implications. Journal of Geology
710 104(4): 417−433.
711 Bröcker M, Klemd R, Cosca M, Brock W, Larionov AN, Rodionov N (2009) The timing of
712 eclogite facies metamorphism and migmatization in the Orlica-Śnieżnik complex,

713 Bohemian Massif: Constraints from a multimethod geochronological study. Journal of
714 Metamorphic Geology 27(5): 385−403.
715 Bröcker M, Klemd R, Kooijman E, Berndt J, Larionov A (2010) Zircon geochronology and
716 trace element characteristics of eclogites and granulites from the Orlica-Śnieżnik complex,
717 Bohemian Massif. Geological Magazine 147(3): 339−362.
718 Brown M, Solar GS (1998) Shear-zone and melts: feedback relations and self-organization in
719 orogenic belts. Journal of Structural Geology 20(2-3): 211–227.
720 Brown M (2007) Metamorphic conditions in orogenic belts: A record of secular change.
721 International Geology Review 49(3): 193–234.
722 Budzyń B, Jastrzębski M, Kozub-Budzyń G, Konečyń P (2015) Monazite Th–Utotal–Pb
723 geochronology and *P–T* thermodynamic modelling in a revision of the H*P*–H*T*
724 metamorphic record in granulites from Stary Gierałtów (NE Orlica-Śnieżnik Dome, SW
725 Poland). Geological Quarterly 59: 700–717.
726 Chopin F, Schulmann K, Skrzypek E, Lexa O, Martelat JE, Lehmann J, Corsini M, Dujardin
727 JR, Edel JB, Štípská P, Pitra P (2012a) Crustal influx, indentation, ductile thinning and
728 gravity redistribution in a continental wedge: building a Moldanubian mantled gneiss
729 dome with underthrust Saxothuringian material (European Variscan belt). Tectonics
730 31(TC1013): 1–27.
731 Chopin F, Schulmann K, Štípská P, Martelat, JE, Pitra P, Lexa O, Petri B (2012b)
732 Microstructural and metamorphic evolution of a high pressure granitic orthogneiss during
733 continental subduction (Orlica-Śnieżnik dome, Bohemian Massif). Journal of
734 Metamorphic Geology 30: 347–376. doi:10.1111/j.1525-1314.2011.00970.x
735 Collins WJ, Sawyer EW (1996) Pervasive granitoid magma transfer through the lower-middle
736 crust during non-coaxial compressional deformation. Journal of Metamorphic Geology
737 14: 565–579.

738 Coggon R, Holland TJB (2002). Mixing properties of phengitic micas and revised garnet-
739 phengite thermobarometers. Journal of Metamorphic Geology 20: 683–696.
740 Don J (1964) Góry Złote i Krowiarki jako elementy składowe metamorfiku Śnieżnik (The
741 Złote and Krowiarki Mountians as structural elements of the Śnieżnik metamorphic
742 massif). Geologia Sudetica 1: 79–117.
743 Don J (1982) The Sienna synform and the relationship of gneisses to the deformational stages
744 distinguished in the Śnieżnik metamorphic massif (Sudetes). Geologia Sudetica 17:
745 130−124.
746 Don J, Dumick M, Wojciechowska I, Żelaźmiewicz A (1990) Lithology and tectonics of the
747 Orlica-Śnieżniek Dome, Sudetes – Recent state of knowledge. Neues Jahrbuch für
748 Geologie und Paläeontologie - Abhandlungen. 179(2-3): 159–188.
749 Don J, Skácel J, Gotowała R (2003) The boundary zone of the East and West Sudetes on the
750 1:50000 scale geological map of the Velké Vrbno, Staré Město and Śnieżnik
751 Metamorphic Units. Geologia Sudetica 35(1): 25–59.
752 Evensen NM, Hamilton PJ, O'Nions RK (1978) Rare-earth abundances in chondritic
753 meteorites. Geochimica et Cosmochimica Acta 42: 1199–1212.
754 Ferrero S, Wunder B, Walczak K, O'Brien PJ, Ziemann MA (2015) Preserved near ultrahigh-
755 pressure melt from continental crust subducted to mantle depths. Geology 43: 447–450.
756 Finch M, Hasalová P, Weinberg RF, Fanning CM (2014) Switch from thrusting to normal
757 shearing in the Zanskar shear zone, NW Himalaya: Implications for channel flow.
758 Geological Society of America Bulletin 126(7-8): 892–924.
759 Fischer G (1936) Der Bau des Glatzer Scchneegebirges, Jahrb. Preuss. Geol. Landesanst. 56:
760 712–732.
761 Franke W, Zelaźniewicz A (2000) The eastern termination of the Variscides: Terrane
762 correlation and kinematic evolution. In: Franke W, et al. (eds) Orogenic Processes:

763 Quantification and Modelling in the Variscan Belt. Geological Society Special Publication
764 179: 63–86.
765 Goncalves Ph, Oliot E, Marquer D, Connolly JAD (2012) Role of chemical processes on
766 shear zone formation: an example from the Grimsel metagranodiorite (Aar massif, Central
767 Alps). Journal of Metamorphic Geology 30(7): 703–722.
768 Grant JA (1986) The isocon diagram-a simple solution to Gresens' equation for metasomatic
769 alteration. Economic Geology 81(8): 1976−1982.
770 Hasalová P, Schulmann K, Lexa O, Štípská P, Hrouda F, Ulrich S, Haloda J, Týcová P
771 (2008a) Origin of migmatites by deformation-enhanced melt infiltration of orthogneiss: a
772 new model based on quantitative microstructural analysis. Journal of Metamorphic
773 Geology 26: 29−53.
774 Hasalová P. Janoušek V, Schulmann K, Štípská P, Erban V (2008b) From orthogneiss to
775 migmatite: geochemical assessment of the melt infiltration model in the Gföhl Unit
776 (Moldanubian Zone, Bohemian Massif). Lithos 102: 508−537.
777 Hasalová P, Štípská P, Powell R, Schulmann K, Janoušek V, Lexa O (2008c) Transforming
778 mylonitic metagranite by open-system interactions during melt flow. Journal of
779 Metamorphic Geology 26: 55−80.
780 Holland TJB, Powell R (1998) An internally consistent thermodynamic data set for phases of
781 petrological interest. Journal of Metamorphic Geology 16: 309–343.
782 Holland TJB, Powell R (2003). Activity-composition relations for phases in petrological
783 calculations: an asymmetric multicomponent formulation. Contributions to Mineralogy
784 and Petrology 145: 492–501.
785 Hollister LS (1993) The role of melt in the uplift and exhumation of orogenic belts. Chemical
786 Geology 108: 31–48.

787 Hopkins MB, Harrison TM, Manning CE (2010) Constraints on Hadean geodynamic from
788 mineral inclusions in >4 Ga zircons. Earth and Planetary Science Letters 298: 367–376.
789 Jastrzębski M (2009) A Variscan continental collision of the West Sudetes and the
790 Brunovistulian terrane: A contribution from structural and metamorphic record of the
791 Stronie Formation, the Orlica-Śnieżnik Dome, SW Poland. International Journal of Earth
792 Sciences 98: 1901–1923.
793 Jastrzębski M, Żelaźniewicz A, Nowak I, Murtezi M, Larionov AN (2010) Protolith age and
794 provenance of metasedimentary rocks in Variscan allochthon units: U–Pb SHRIMP zircon
795 data from the Orlica-Śnieżnik Dome, West Sudetes. Geological Magazine 147(3):
796 416−433.
797 Jastrzebski M, Budzyń B, Stawikowski W (2017) Cambro-Ordovician vs Devono-
798 Carboniferous geodynamic evolution of the Bohemian Massif: evidence from P–T–t
799 studies in the Orlica-Śnieżnik Dome, SW Poland. Geological Magazine 156(3): 447–470.
800 Jedlička R, Faryad SW (2017) Felsic granulite with layers of eclogite facie rocks in the
801 Bohemian Massif; did they share a common metamorphic history? Lithos 286-287: 408–
802 425.
803 Klemd R, Bröcker M, Schramm J (1995) Characterization of amphibolite-facies fluids of
804 Variscan eclogites from the Orlica-Śnieżnik dome (Sudetes, SW Poland). Chemical
805 Geology 119: 101–113.
806 Klemd R, Bröcker M (1999) Fluid influence on mineral reactions in ultrahigh-pressure
807 granulites: a case study in the Śnieżnik Mts. (West Sudetes, Poland). Contributions to
808 Mineralogy and Petrology 136(4): 358−373.
809 Kozłowski K (1961) Kompleks granulitowy Starego Gierałtowa w Górach Złotych (The
810 granulitic complex of Stary Gierałtow – East Sudetes). Archive of Mineralogy 25: 5–123.

Kröner A, Štípská P, Schulmann K, Jaeckel P (2000) Chronological constraints on the pre-Variscan evolution of the Northeastern margin of the Bohemian Massif, Czech Republic. In: Franke W, et al. Orogenic Processes; Quantification and Modelling in the Variscan Belt. Geological Society Special Publication 179: 175–197.

Kröner A, Jaeckel P, Hegner E, Opletal M (2001) Single zircon ages and whole rock Nd isotopic systematics of early Palaeozoic granitoid gneisses from the Czech and Polish Sudetes (Jizerské hory, Krkonoše Mountains and Orlice-Śnieżnik Complex). International Journal of Earth Sciences 90: 304–324.

Kryza R, Pin C, Vielzeuf D (1996) High-pressure granulites from the Sudetes (South-west Poland): Evidence of crustal subduction and collisional thickening in the Variscan Belt. Journal of Metamorphic Geology 14: 531–546.

Lange U, Bröcker M, Mezger K, Don J (2002) Geochemistry and Rb–Sr geochronology of a ductile shear zone in the Orlica-Śnieżnik dome (West Sudetes, Poland). International Journal of Earth Sciences 91(6): 1005−1016.

Lange U, Bröcker M, Armstrong R, Zelazniewicz A, Trapp E, Mezger K (2005) The orthogneiss of the Orlica-Śnieżnik complex (West Sudetes, Poland): geochemical characteristics, the importance of pre-Variscan migmatization and constraints on the cooling history. Journal of the Geological Society 162: 973−984.

Lehmann J, Schulmann K, Edel JB, Ježek J, Hrouda F, Lexa O, Chopin F (2013) Structural and anisotropy of magnetic susceptibility records of granitoids sheets emplacement during growth of a continental gneiss dome (Central Sudetes, European Variscan Belt). Tectonics 32: 1–23.

Lehmann J, Schulmann K, Lexa O, Závada P, Štípská P, Hasalová P, Belyanin G, Corsini M (2017) Detachment folding of partially molten crust in accretionary orogens: A new magma-enhanced vertical mass and heat transfer mechanism. Lithosphere 9(6): 889–909.

836 Lexa O, Schulmann K, Janoušek V, Štípská P, Guy A, Racek M (2011) Heat sources and
837 trigger mechanisms of exhumation of H*P* granulites in Variscan orogenic root. Journal of
838 Metamorphic Geology 29: 79–102.
839 Lopez-Moro FJ (2012) EASYGRESGRANT – A Microsoft Excel spreadsheet to quantify
840 volume changes and to perform mass-balance modelling in metasomatic systems:
841 Computer and Geosciences 39: 191–196.
842 Maierová P, Lexa O, Schulmann K, Štípská P (2014) Contrasting tectono-metamorphic
843 evolution of orogenic lower crust in the Bohemian Massif: A numerical mode. Gondwana
844 Research 25(2): 509–521.
845 Maluski H, Rajlich P, Souček J (1995) Pre-Variscan, Variscan and early Alpine thermos-
846 tectonic history of the northeastern Bohemian Massif: 40Ar/39Ar study. Geologische
847 Rundschau 84: 345–358.
848 Marquer D, Burkhard M (1992) Fluid circulation, progressive deformation and mass-transfer
849 processes in the upper crust: the example of basement-cover relationships in the External
850 Crystalline Massifs, Switzerland. Journal of Structural Geology 14(8−9): 1047−1057.
851 Mazur S, Aleksandrowski P (2001) The Tepla(?)/Saxothuringian suture in the Karkonosze-
852 Izera massif , Western Sudetes, Central European Variscides, Internacional Journal of
853 Earth Sciences 90(2): 341–360.
854 Mazur S, Kröner A, Szczepański J, Turniak K, Hanžl P, Melichar R, Rodionov NV, Paderin I,
855 Sergeev SA (2010) Single zircon U–Pb ages and geochemistry of granitoid gneisses from
856 SW Poland: Evidence for an Avalonian affinity of the Brunian microcontinent. Geological
857 Magazine 174(4): 508–526.
858 Mazur S, Szczepański J, Turniak K, McNaughton N (2012) Location of the Rheic suture in
859 the eastern Bohemian Massif: Evidence from detrital zircon data. Terra Nova 24: 199–
860 206.

Murtezi M (2006) The acid metavolcanic rocks of the Orlica-Śnieżnik Dome (Sudete): Their origin and tectono-metamorphic evolution. Geologia Sudetica 38: 1–38.

Nahodilová R, Štípská P, Powell R, Košler J, Racek M (2014) High-Ti muscovite as a prograde relict in high pressure granulites with metamorphic Devonian zircon ages (Běstvina granulite body, Bohemian Massif): Consequences for the relamination model of subducted crust. Gondwana Research 258: 630–648.

Oliot E, Goncalves Ph, Schulmann K, Marquer D, Lexa O (2014) Mid-crustal shear zone formation in granitic rocks: Contraints from quantitative textural and crystallographic preferred orientations analyses. Tectonophysics 612-613: 63–80.

Oliver GJH, Corfu F, Krogh TE (1993) U–Pb ages from SW Poland: Evidence for a Caledonian suture zone between Baltica and Gondwana. Journal of Geology Society 150: 355–369.

Potdevin JL, Marquer D (1987) Quantitative methods for the estimation of mass transfers by fluids in deformed metamorphic rocks (Méthodes de quantification des transferts de matiére par les fluids dans les roches métamorphiques déformées). Geodinamica Acta 1: 193–206.

Pouba Z, Paděra K, Fiala J (1985) Omphacite granulite from the NE margin of the Bohemian Massif (Rychleby Mountains). Neus Jahrbuch für Mineralogie - Abhandlungen 151: 29–52.

Powell R, Holland TJB, Worley B (1998) Calculating phase diagrams involving solid solutions via non-linear equations, with examples using THERMOCALC. Journal of Metamorphic Geology 16: 577–588.

Pressler RE, Schneider DA, Petronis MS, Holm DK, Geissman JW (2007) Pervasive horizontal fabric and rapid vertical extrusion: Lateral overturning and margin sub-parallel

885 flow of deep crustal migmatites, northeastern Bohemian Massif. Tectonophysics 443(1-2):
886 19–36.
887 Rosenberg CL, Handy M (2005) Experimental deformation of partially melted granite
888 revisited: Implications for the continental crust. Journal of Metamorphic Geology 23: 19–
889 28.
890 Schneider DA, Zahniser SJ, Glascock JM, Gordon SM, Manecki M (2006)
891 Thermochronology of the West Sudetes (Bohemian Massif): Rapid and repeated eduction
892 in the Eastern Variscides, Polamd and Czech Republic. American Journal Science
893 306(10): 846–873.
894 Schulmann K, Martelat J-E, Ulrich S, Lexa O, Štípská P, Becker JK (2008) Evolution of
895 microstructure and melt topology in partially molten granitic mylonite: Implications for
896 rheology of felsic middle crust. Journal of Geophysical Research-Solid Earth 113(B10).
897 Skrzypek E, Schulmann K, Štípská P, Chopin F, Lehmann J, Lexa O, Haloda J (2011a)
898 Tectono-metamorphic history recorded in garnet porphyroblasts: Insights from
899 thermodynamic modelling and electron backscatter diffraction analysis of inclusion trails.
900 Journal of Metamorphic Geology 29: 473–496.
901 Skrzypek E, Štípská P, Schulmann K, Lexa O, Lexová M, (2011b) Prograde and retrograde
902 metamorphic fabrics – a key for understanding burial and exhumation in orogens
903 (Bohemian Massif). Journal of Metamorphic Geology 29: 451–472.
904 Skrzypek E, Lehmann J, Szczepański J, Anczkiewicz R, Štípská P, Schulmann K, Kröner A,
905 Białek D (2014) Time-scale of deformation and intertectonic phases revealed by *P–T–D–t*
906 relationships in the orogenic middle crust od the Orlica-Śnieżnik Dome, Polish/Czech
907 Central Sudetes. Journal of Metamorphic Geology 32: 981–1003.
908 Smulikowski K (1967) Eklogite Gór Śnieznickich w Sudetach (Eclogites of the Śnieżnik
909 Mountains in the Sudetes). Geologia Sudetica 3: 157–174.

910 Steltenpohl MG, Cymerman Z, Krogh EJ, Kunk MJ (1993) Exhumation of eclogitized
911 continental basement collapse, Sudety Mountains, Poland. Geology 21: 1111–1114.
912 Štípská P, Schulmann K, Kröner A (2004) Vertical extrusion and middle crustal spreading of
913 omphacite granulite: A model of syn-convergent exhumation (Bohemian Massif, Czech
914 Republic). Journal of Metamorphic Geology 22(3): 179−198.
915 Štípská P, Powell R (2005) Does ternary feldspar constrain the metamorphic conditions of
916 high-grade meta-igneous rocks? Evidence from orthopyroxene granulites, Bohemia
917 Massif. Journal of Metamorphic Geology 23: 627–647.
918 Štípská P, Schulmann K, Powell R (2008) Contrasting metamorphic histories of lenses of
919 high-pressure rocks and host migmatites with a flat orogenic fabric (Bohemian Massif,
920 Czech Republic): A result of tectonic mixing within horizontal crustal flow? Journal of
921 Metamorphic Geology 26: 623–646.
922 Štípská P, Chopin F, Skrzypek E, Schulmann K, Lexa O, Pitra P, Martelat J-E, Bolinger C,
923 Žáčková E (2012) The juxtaposition of eclogite and mid-crustal rocks in the Orlica-
924 Śnieżnik Dome, Bohemian Massif. Journal of Metamorphic Geology 30(2): 231–234.
925 doi:10.1111/j.1525-1314.2011.00964.x.
926 Štípská P, Hasalová P, Powell R, Závada P, Schulmann K, Racek M, Aguilar C, Chopin F
927 (2019) The effect of melt infiltration on metagranitic rocks: The Śnieżnik Dome,
928 Bohemian Massif. Journal of Petrology 60: 591–618.
929 Stuart CA, Piazolo S, Daczko NR (2018) The recognition of former melt flux through high-
930 strain zones. Journal of Metamorphic Geology 00: 1–21.
931 Thompson AB, Schulmann K, Jezek J (1997a) Extrusion tectonics and elevation of lower
932 crustal metamorphic rocks in convergent orogens. Geology 25(6): 491–496.
933 Thompson AB, Schulmann K, Jezek J (1997b) Thermal evolution and exhumation in
934 obliquely convergent (transpressive) orogens. Tectonophysics 280: 171–184.

935 Turniak K, Mazur S, Wysoczański R (2000) SHRIMP zircon geochronology and
936 geochemistry of the Orlica-Śnieżnik gneisses (Variscan belt of Central Europe) and their
937 tectonic implications. Geodinamia Acta 13: 293–312.
938 Vanderhaeghe O (2001) Melt segregation, pervasive melt migration and magma mobility in
939 the continental crust: The structural record from pores to orogens. Physic and Chemistry
940 of the Earth (A) 26(4-5): 213–223.
941 Vangerow EF (1943) Das Normalprofil des Algonkium und Kambriums in den mittleren
942 Sudeten. Geologische Rundschau 34: 10–12.
943 Weinberg RF (1999) Mesoscale pervasive felsic magma migration: alternative to dyking.
944 Lithos 46: 393–410.
945 White RW, Pomroy E, Powell R (2005) An in situ metatexite-diatexite transition in upper
946 amphibolite facies rocks from Broken Hill, Australia. Journal of Metamorphic Geology
947 23: 579–602.
948 White RW, Powell R, Holland TJB (2007) Progress relating to calculation of partial melting
949 equilibria for metapelites. Journal of Metamorphic Geology 25: 511–527.
950 Young DJ, Kylander-Clark ARC (2015) Does continental crust transform during eclogite
951 facies metamorphism? Journal of Metamorphic Geology 33: 331–357.
952 Závada P, Schulmann K, Konopasek J, Ulrich S, Lexa O (2007) Extreme ductility of feldspar
953 aggregates - Melt-enhanced grain boundary sliding and creep failure: Rheological
954 implications for felsic lower crust. Journal of Geophysical Research-Solid Earth 112.
955 Závada P, Schulmann K, Racek M, Hasalová P, Jeřábek P, Weinberg RF, Štípská P, Roberts
956 Al (2018) Role of strain localization and melt flow on exhumation of deeply subducted
957 continental crus. Lithosphere 10(2): 217–238.
958 Żelaźniewicz A, Mazur S, Szczepański J (2002) The Ladek-Śnieżnik Metamorphic Unit-
959 Recent state of Knowledge. Geolines 14: 115–125.

960 Żelaźniewicz A, Nowak I, Larionov A, Presnyakov S (2006) Syntectonic Lower Ordovician
961 migmatite and post-tectonic Upper Viséan syenite in the Western limb of the Orlica-
962 Śnieżnik Dome, West Sudetes: U–Pb SHRIMP data from zircons. Geologia Sudetica, 38:
963 63–80.

964 **FIGURE AND TABLE CAPTIONS**

965 **Fig. 01.** (a) Lithotectonic map of North European Variscan belt (modified after
966 Aleksandrowski et al. 1997; Don et al. 2003, Żelaźniewicz et al. 2006). The position of
967 Orlica-Śnieżnik Dome is outlined. (b) Geological sketch map of the Orlica-Śnieżnik Dome
968 (modified after Aleksandrowski et al. 1997; Don et al. 2003; Żelaźniewicz et al. 2006). (c)
969 Geological and structural map of Międzygórze and Králíky-Śnieżnik antiforms (lithologies
970 after Don et al. 2003; Chopin et al. 2012a,b; Štípská et al. 2012). The location of the
971 migmatitic orthogneiss used in this study and the position of the structural profiles are
972 indicated.

973 **Fig. 02.** Interpretative cross-sections showing the main structural relationships between both
974 antiforms (a-b) and the different orthogneiss types. See Figure 1c for locations of profiles.

975 **Fig. 03.** Outcrop photograph illustrating a lithological sketch (see legend in the Figures 1 and
976 2) and the locations of studied samples with white stars. Field photographs showing the
977 different textural rocks displayed, ranging from augen to banded and fine-grained migmatitic
978 orthogneiss.

979 **Fig. 04.** Textural features of the different types of orthogneiss and migmatitic rocks (SEM
980 BSE images). Augen to banded type II: alternation of almost monomineral layers of
981 recrystallized K-feldspar, quartz and plagioclase distinctly defined. Banded type II:
982 alternation of almost monomineral layers of recrystallized K-feldspar, quartz and plagioclase
983 with highly diffuse boundary between feldspar layers. Schlieren migmatite characterised by

relics of K-felsdpar-rich layers in otherwise isotropic matrix. Nebulitic migmatite with no relics of original banding. Grey colour scale corresponds to variation in chemical components, i.e. with increasing white intensity: void, quartz, plagioclase, K-feldspar, white micas and biotite/garnet (not distinguished). All pictures are at the same scale.

Fig. 05. Detailed back scattered electron (BSE) images of different rock types. (a) Diffuse boundary between a layers of mixed aggregates and a K-feldspar-rich layer with numerous interstitial plagioclase, quartz and myrmekite. (b) Detail of cuspate plagioclase and rounded quartz as interstitial phases in K-feldspar layer. (c) Quartz- and plagioclase-rich layers with interstitial grains of feldspar and quartz. Phengite is surrounded by biotite and biotite occurs also along cleavage of phengite. (d) Large crystal of plagioclase with and antiperthitic core rich in exsolutions of K-feldspar. (e) Large phengite laths with biotite at margins and along the cleavage. (f) Garnet in a matrix of quartz, plagioclase, K-feldspar, phengite, biotite and myrmekite. (g) Symplectite of quartz and white mica at the boundary of K-feldspar and phengite.

Fig. 06. Composition of feldspar for the different rock types localized in different microstructural positions (a−g). Representative analyses are listed in Table 1.

Fig. 07. Composition of white mica: (a) Si (p.f.u.) content of white micas *v*. rock types. Note the decrease in Si (p.f.u.) content from cores to rim. (b−c) Compositional ranges from cores to rims of white micas. Grey arrows indicate zoning from core to rim. Representative analyses are listed in Table 2.

Fig. 08. Composition of biotite for the different rock types (a, b). Representative analyses are listed in Table 2.

Fig. 09. Garnet compositional trends of the different rock types: (a) augen to banded type II (sample FC076B); (b) banded type II (sample FC076E); (c) schlieren migmatite (sample FC076J): and (d) nebulitic migmatite (FC076C). Representative analyses are listed in Table 3.

Fig. 10. Isocon diagrams after Grant (1986) comparing: (a) the whole-rock compositions of banded type II to nebulitic migmatite (vertical axis) with respect to the augen-banded type II composition. The diagram (a) shows loss and/or gain of elements with respect to composition of reference rock plotted as reference line. (b) Spider plot normalized to chondrite (Evensen et al. 1978). Shaded field corresponds to the orthogneiss types described by Chopin et al. (2012b) in the Międzygórze antiform. (c) Spider plot normalized to augen-banded type II (sample FC076A).

Fig. 11. Potdevin diagrams (Potdevin and Marquer, 1987; Lopez-Moro, 2012) illustrating the loss-gain relationships for a range of incompatible elements for banded type II, schlieren and nebulitic migmatites compared to augen-banded type II. LILE = Large Ion Lithophile Elements, HFSE = High Field Strength Elements, REE = Rare Earth Elements. (see Table 5).

Fig. 12. *P*-*M*(H_2O) pseudosection calculated at 7 kbar for a nebulitic migmatite (sample FC076C) and contoured for the calculated spessartine (m(sps)), almandine (x(alm)) and grossular (z(grs)) contents of garnet and for the molar proportion of liquid (liq (mol. %)). The solidus is emphasized by a dark-dashed line. Quartz, plagioclase and K-feldspar are present in all fields.

Fig. 13. (a) *P–T* pseudosection calculated for the analysed whole-rock composition of a nebulitic migmatite (sample FC076C). (b−e) Simplified pseudosections with compositional isopleths of spessartine (m(sps)), almandine (x(alm)) and grossular (z(grs)) in garnet; Si content of white mica (Si(wm) p.f.u.); anorthite content of plagioclase (ca(pl)); and molar proportion of melt (liq (mol. %)). The ellipses indicate the *P–T* ranges compatible with the observed assemblage and core and rim compositions of garnet and white mica. The star

indicates *P–T* conditions from which the melt composition was taken to be reintegrated into whole-rock composition shown in Figures 14 and 15. The solidus is underlined by a thick black dashed line. See text for discussion of the *P–T* path.

Fig. 14. $T–X_{melt}$ pseudosection calculated at 700 °C for a range of compositions representing mixtures of H_2O-undersaturated whole-rock composition of the nebulitic migmatite (x = 0) and the composition of melt calculated at 680 °C and 16 kbar (x = 1, black star in Figure 13). X_{melt} is the proportion of melt added in the migmatites at 16 kbar. x = 1 corresponds to 20 mol. % of melt added. The solidus is underlined by a thick black dashed line. The calculated isopleths show molar proportion of garnet (g mol. %), almandine (x(alm)) and grossular (z(grs)) content of garnet, Si content of white micas (Si(wm) p.f.u.) and molar proportion of melt (liq mol. %). The ellipses indicate the *P–T* ranges compatible with the observed assemblage and core and rim compositions of garnet and white mica. Evolution along three decompression paths at different X_{melt} is discussed in the text.

Fig. 15. (a) *P–T* pseudosection calculated with 3.40 mol. % melt added to the whole-rock composition of the nebulitic migmatite. (b−e) Simplified pseudosections with compositional isopleths of spessartine (m(sps)), almandine (x(alm)) and grossular (z(grs)) in garnet; Si content of muscovite (Si(wm) p.f.u.); anorthite content of plagioclase (ca(pl)); and molar proportion of melt (liq (mol. %)). The ellipses indicate the *P–T* ranges compatible with the observed assemblage and core and rim compositions of garnet and white mica. The solidus is underlined by a thick black dashed line. See text for discussion of the *P–T* path.

Fig. 16. Tectonic sketch of the Orlica-Śnieżnik Dome as a part of the Sudetes showing shallow-dipping S1 fabrics related to subduction of the continental crust up to eclogite- and (U)H*P* granulite-facies conditions, and subvertical S2 fabrics related to its vertical exhumation to the middle and upper crust (modified after Chopin et al. 2012a). Two different positions in subduction wedge are indicated as a proximal part (A) and a more distal part (B)

with respect to the subduction. (A) Międzygórze antiform: melt-absent orthogneiss with local migmatite formation. Shallow-dipping S1 fabric preserved in the low-strain D2 domains. Grain-scale melt percolation is mainly localized in narrow zones of vertical S2 fabric (modified after Štípská et al. 2019). Compilation of *P*–*T* paths for orthogneiss and eclogites reported by Chopin et al. 2012b (1), Štípská et al. 2012 (2), Jastrzebski et al. 2017 (3) and Štípská et al. 2109 (4). (B) Králíky-Śnieżnik antiform: melt-present migmatitic orthogneiss. High-strain D2 domains with subvertical S2 foliation are connected with crustal-scale shear zones. The wide zone of subvertical S2 fabric is to a large extent percolated by melt. Simplified *P*–*T* diagram with the *P*–*T* path obtained in this study. *P*–*T* paths are mostly within the melt-present assemblages.

Table 01. Representative analyses of feldspar.

Table 02. Representative analyses of micas.

Table 03. Representative analyses of garnet.

Table 04. Major and trace-element compositions (ICP-AES and -MS). LOI: Loss On Ignition.

Table 05. Gain/loss of incompatible elements of the studied rocks relative to augen-banded type II (sample FC076A).

Fig.1

Click here to access/download;Figure;Fig01.tif

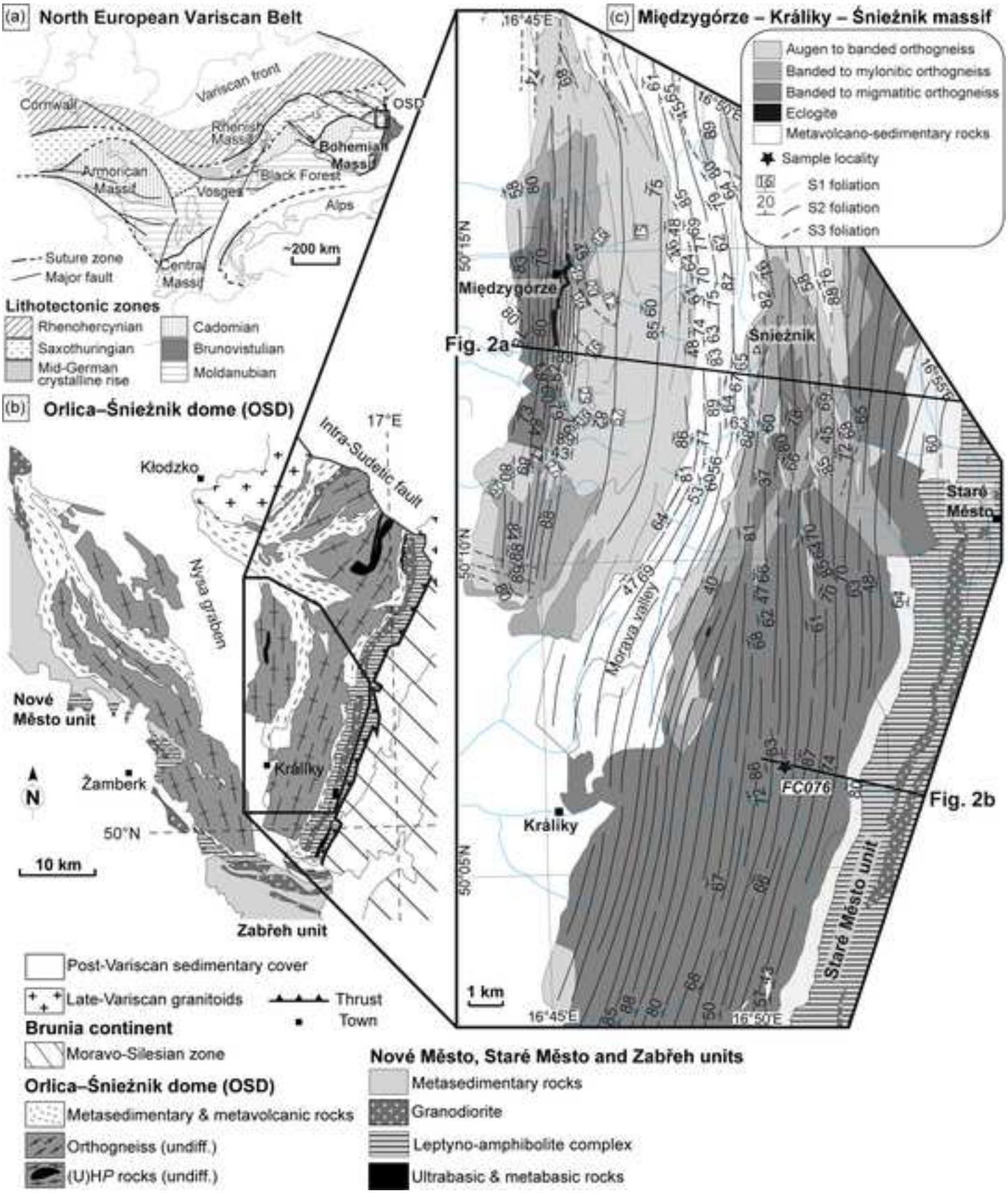

Fig.2

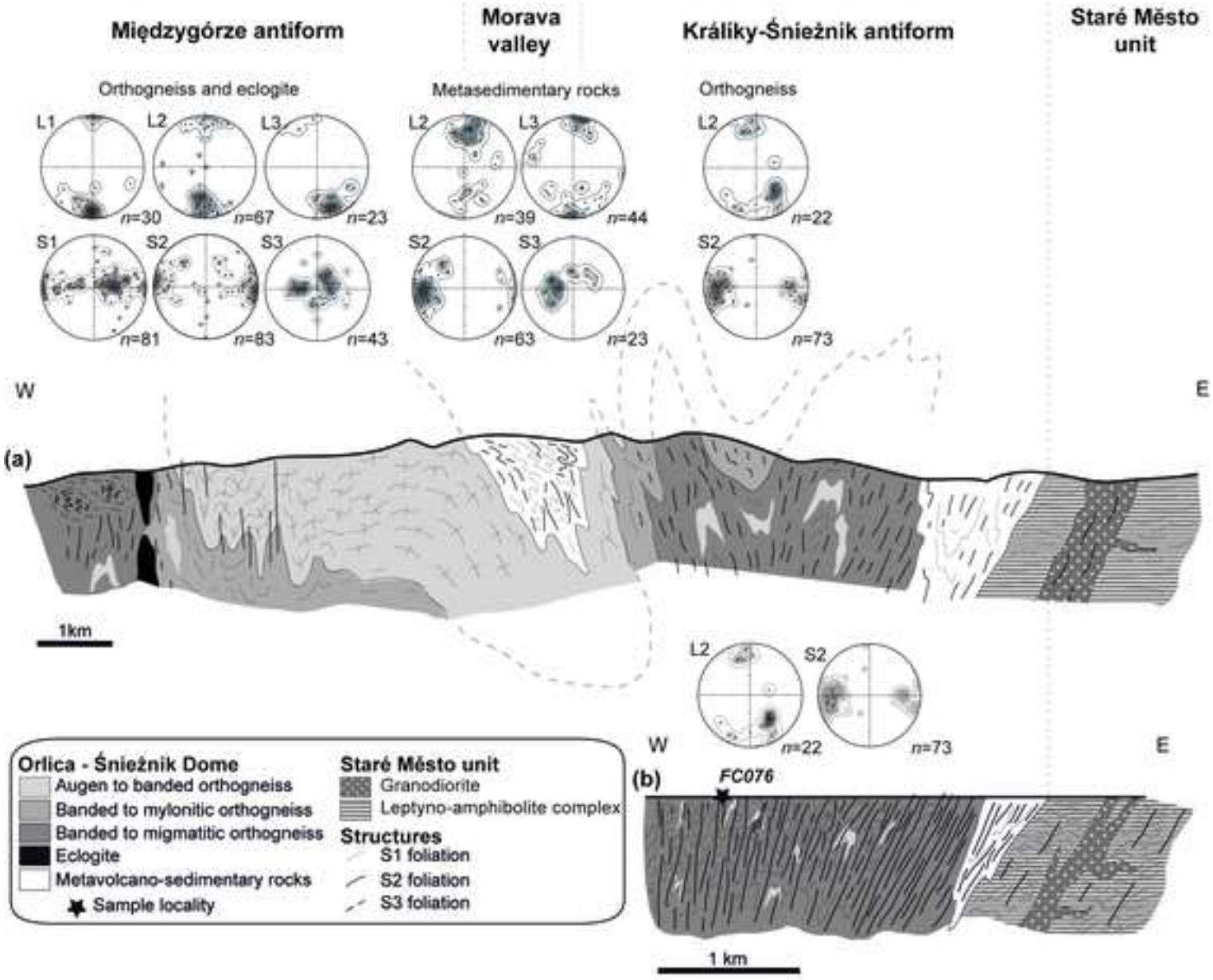

Fig.3

Click here to access/download;Figure;Fig03.tif

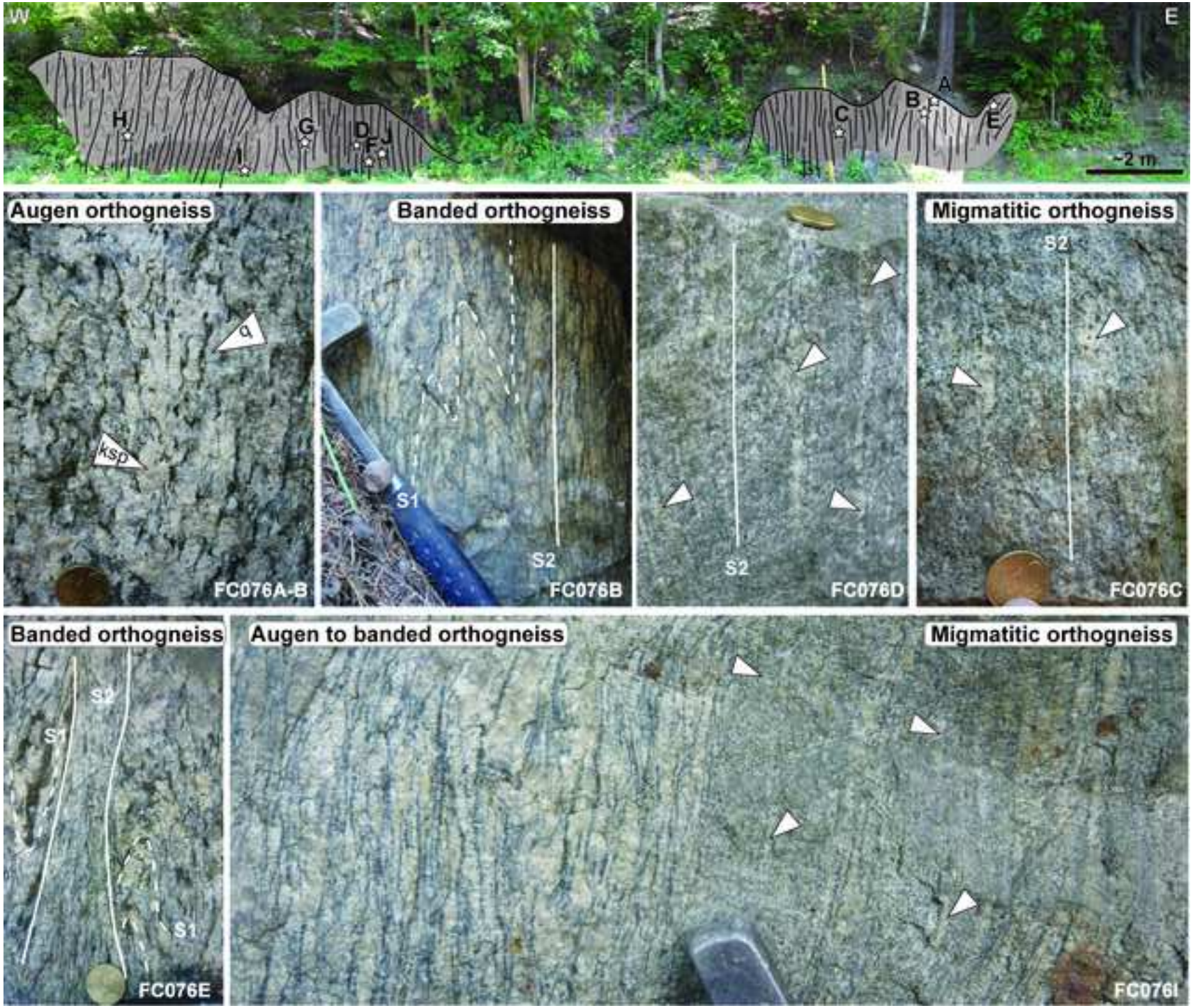

Fig.4

Click here to access/download;Figure;Fig04.tif

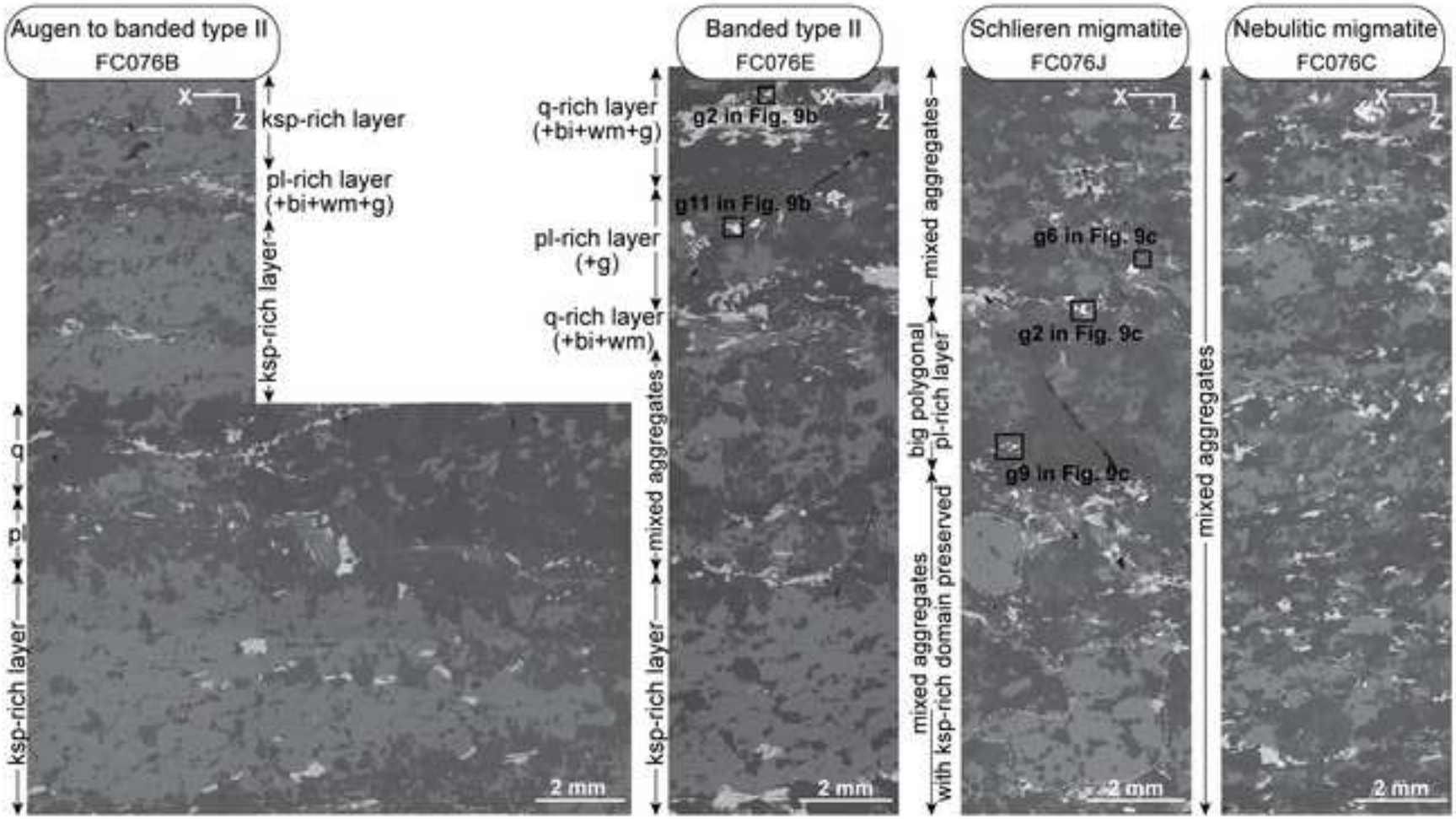

Fig.5

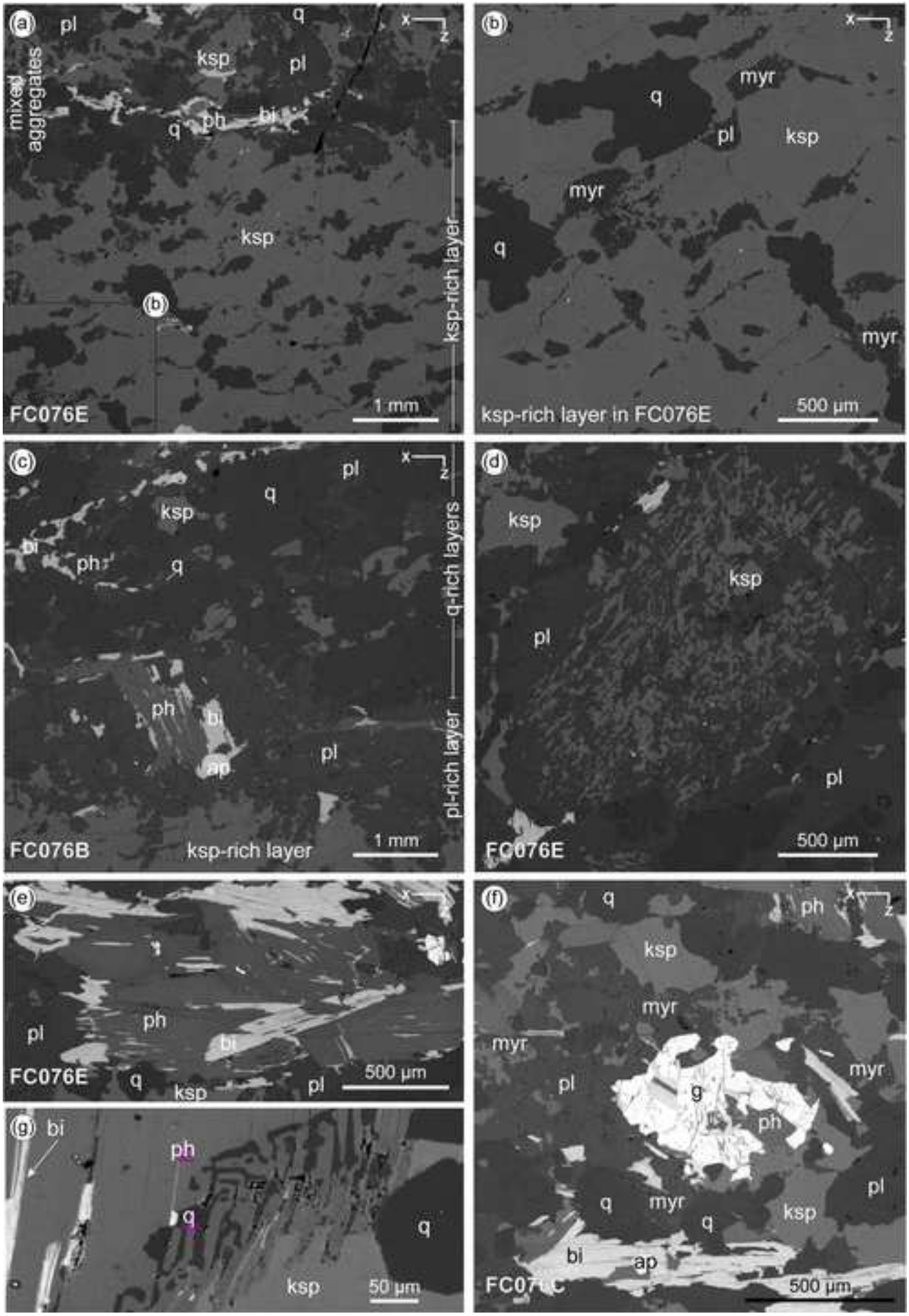

Fig.6

Click here to access/download;Figure;Fig06.tif

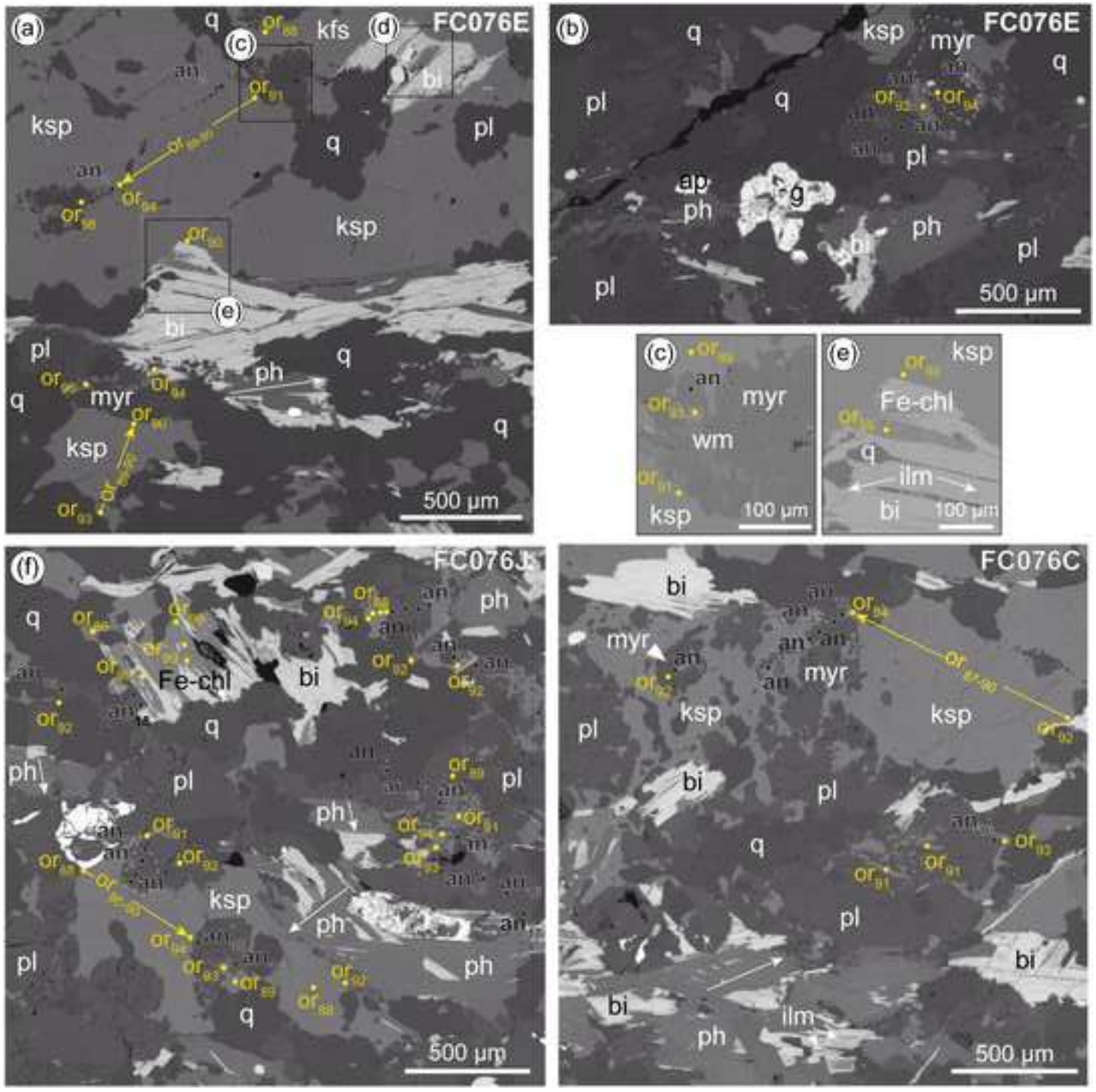

Fig.7

Click here to access/download;Figure;Fig07.tif

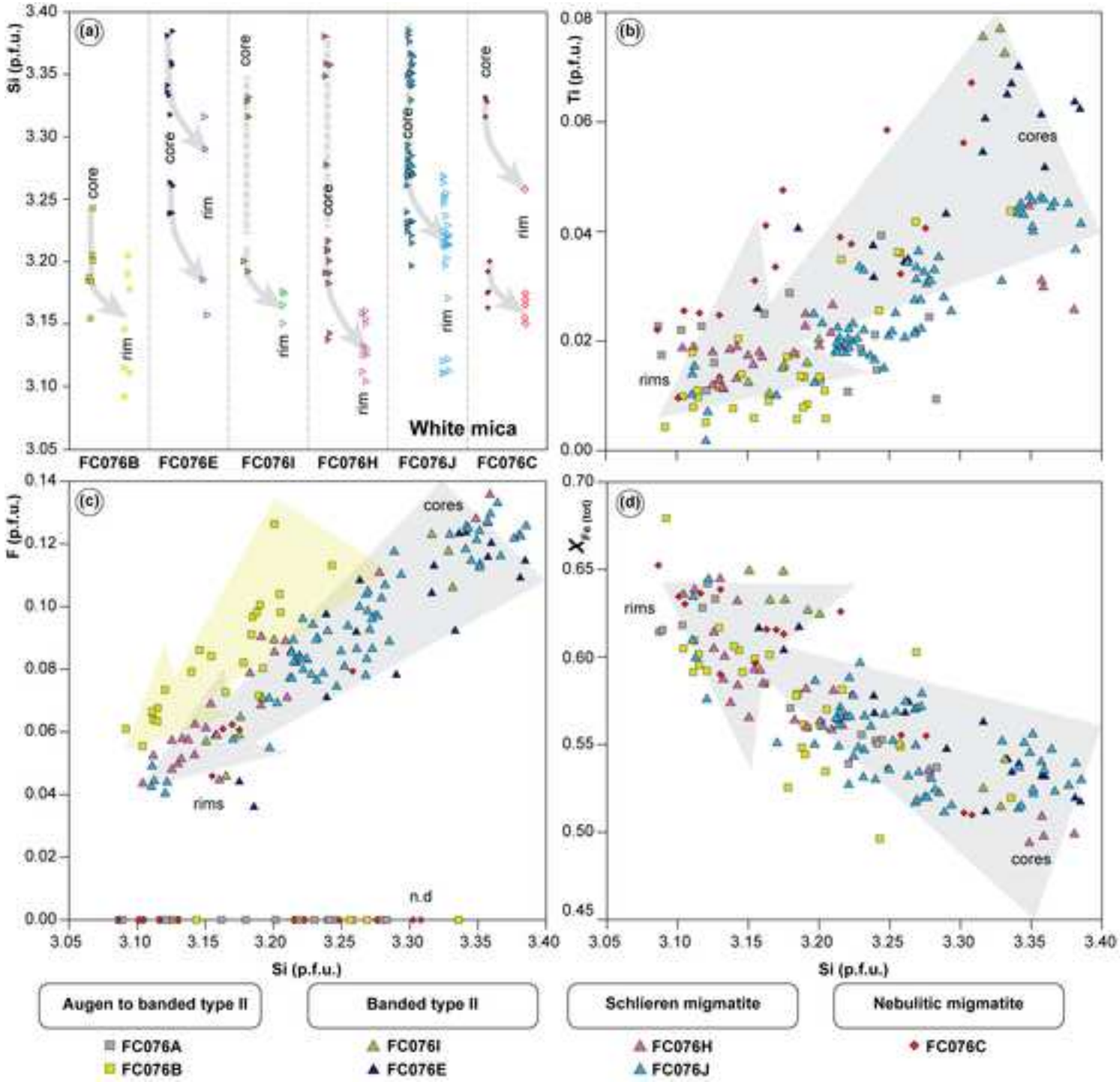

Fig.8

Click here to access/download;Figure;Fig08.tif

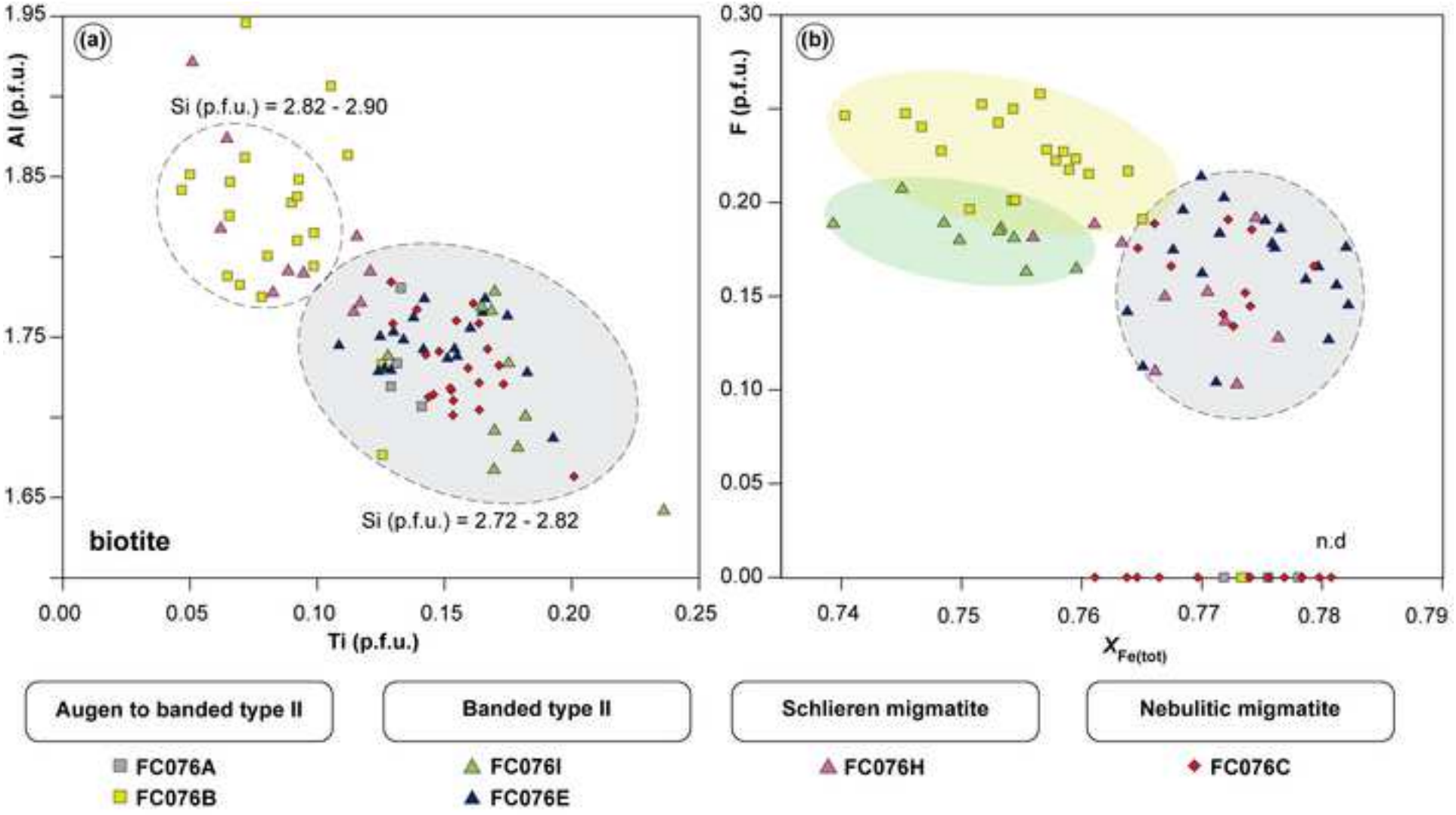

Fig.9

Click here to access/download;Figure;Fig09.tif

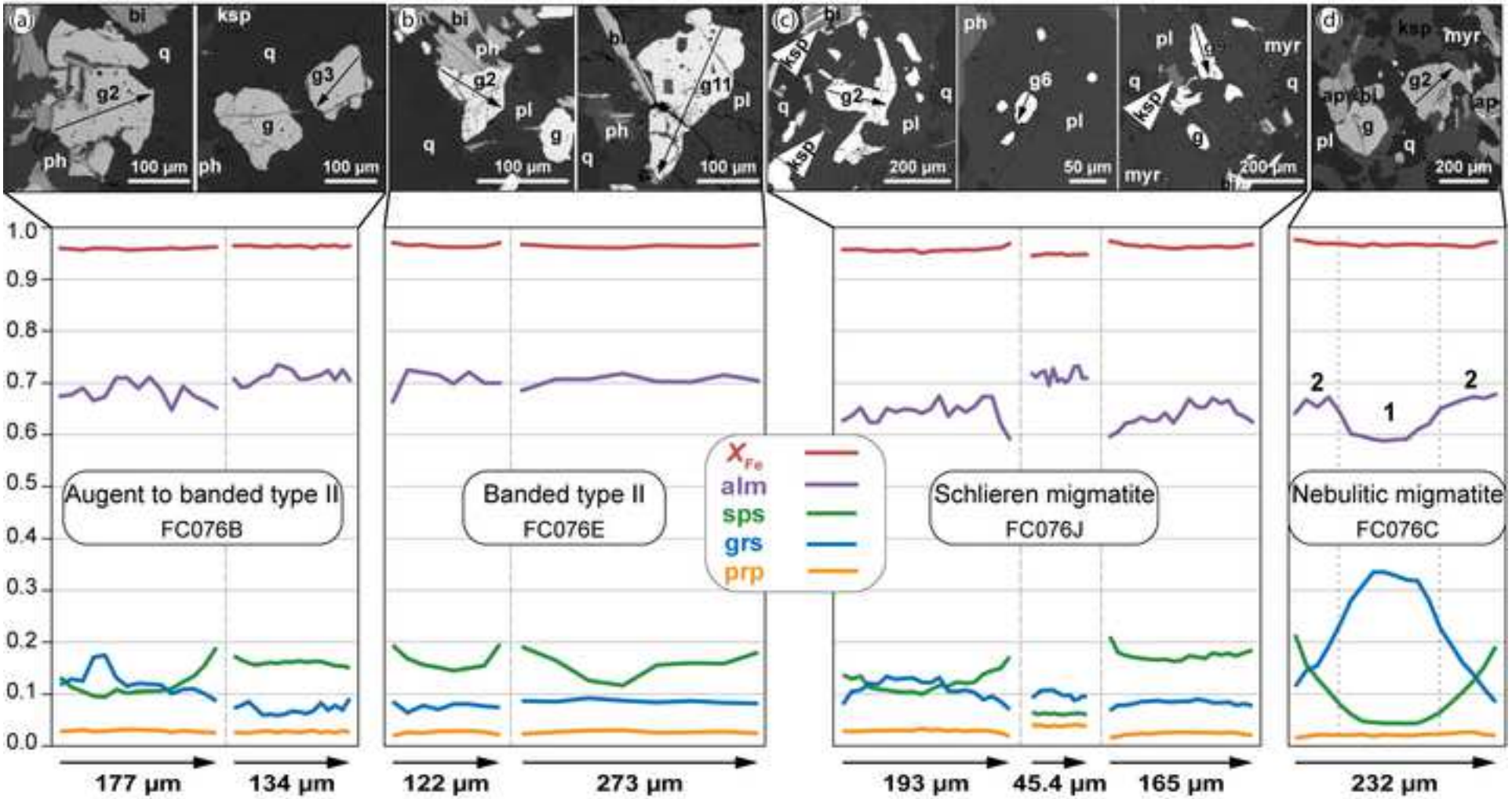

Fig.10

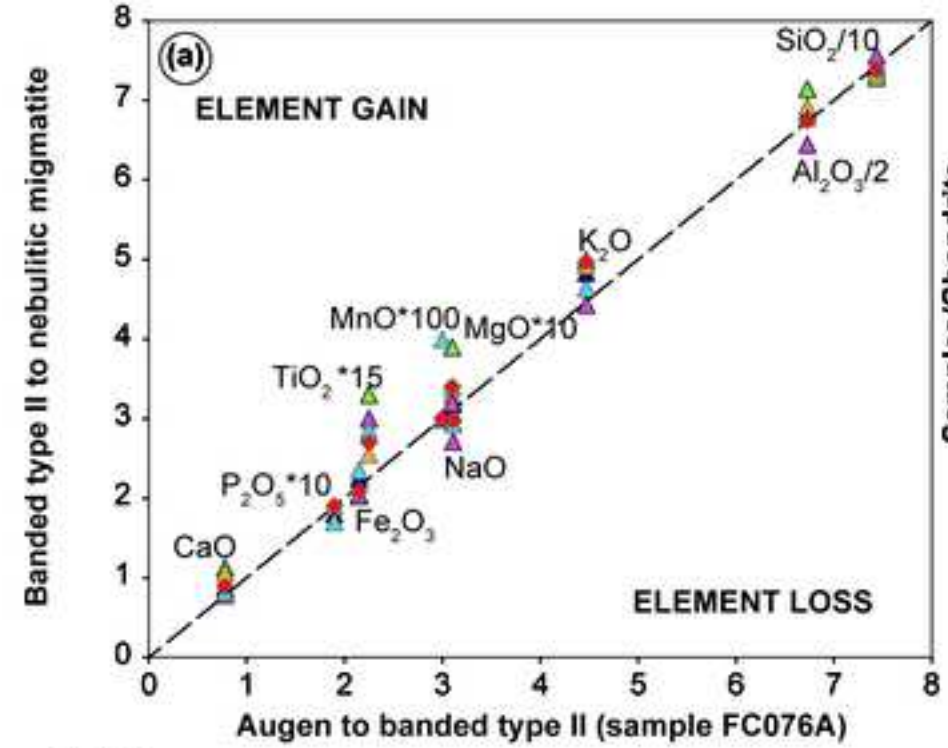

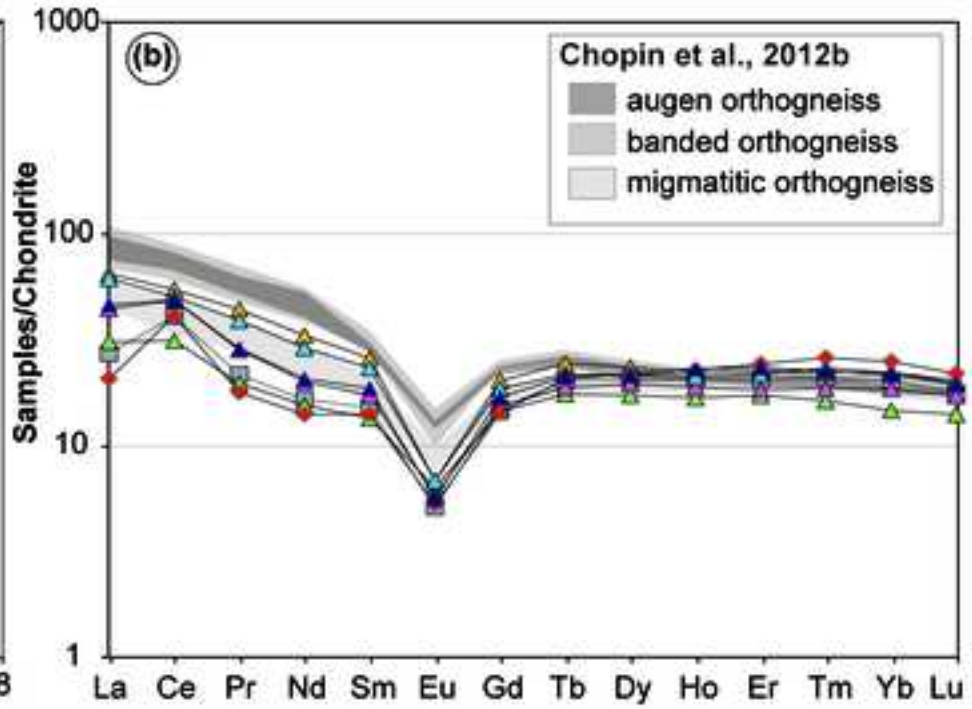

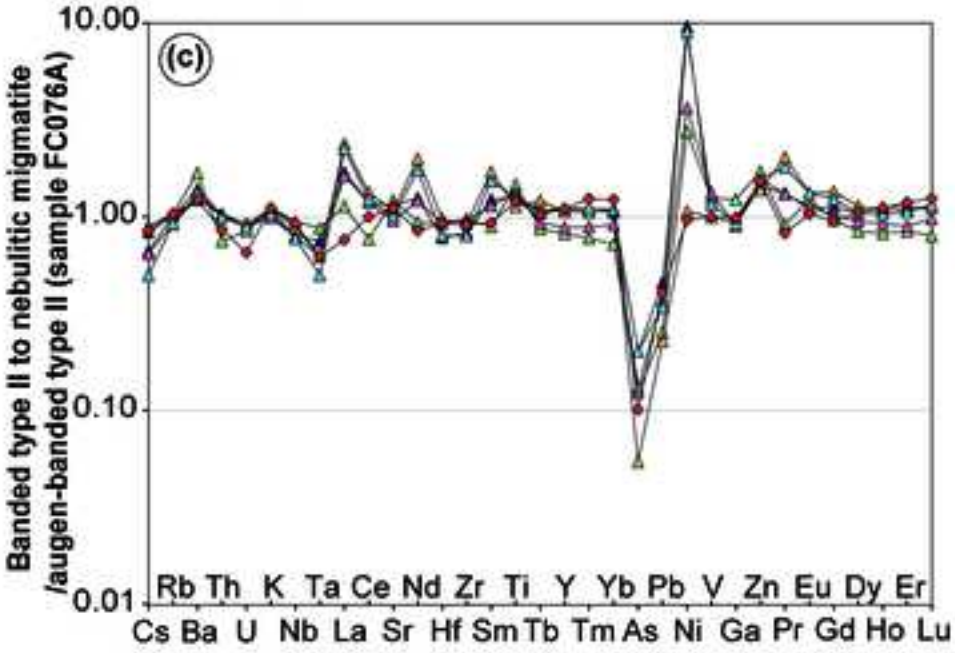

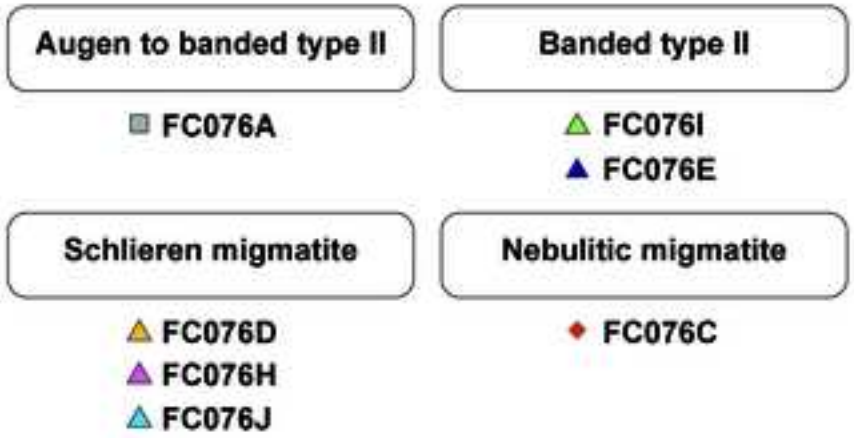

Fig.11

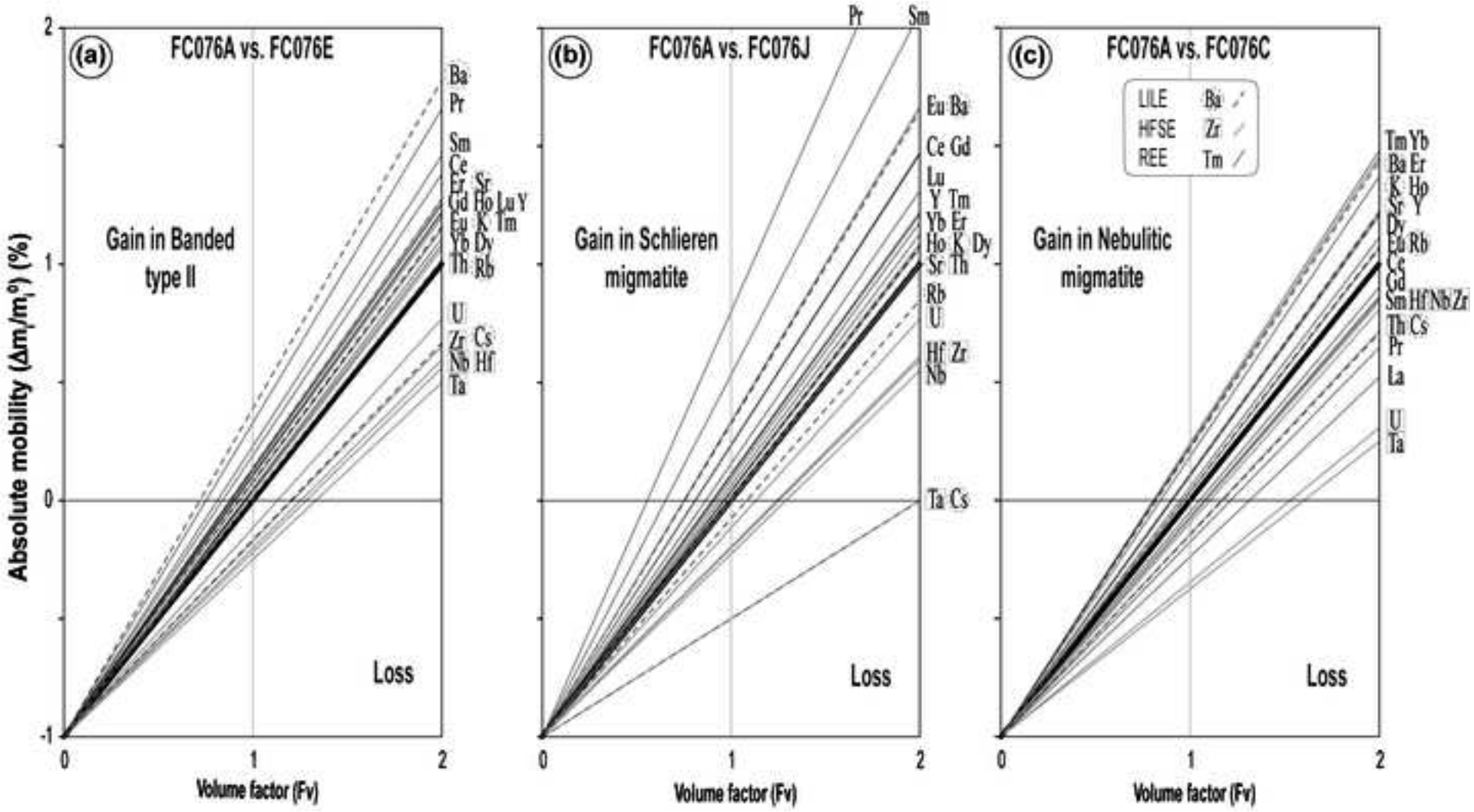

Fig.12

Click here to access/download;Figure;Fig12.tif

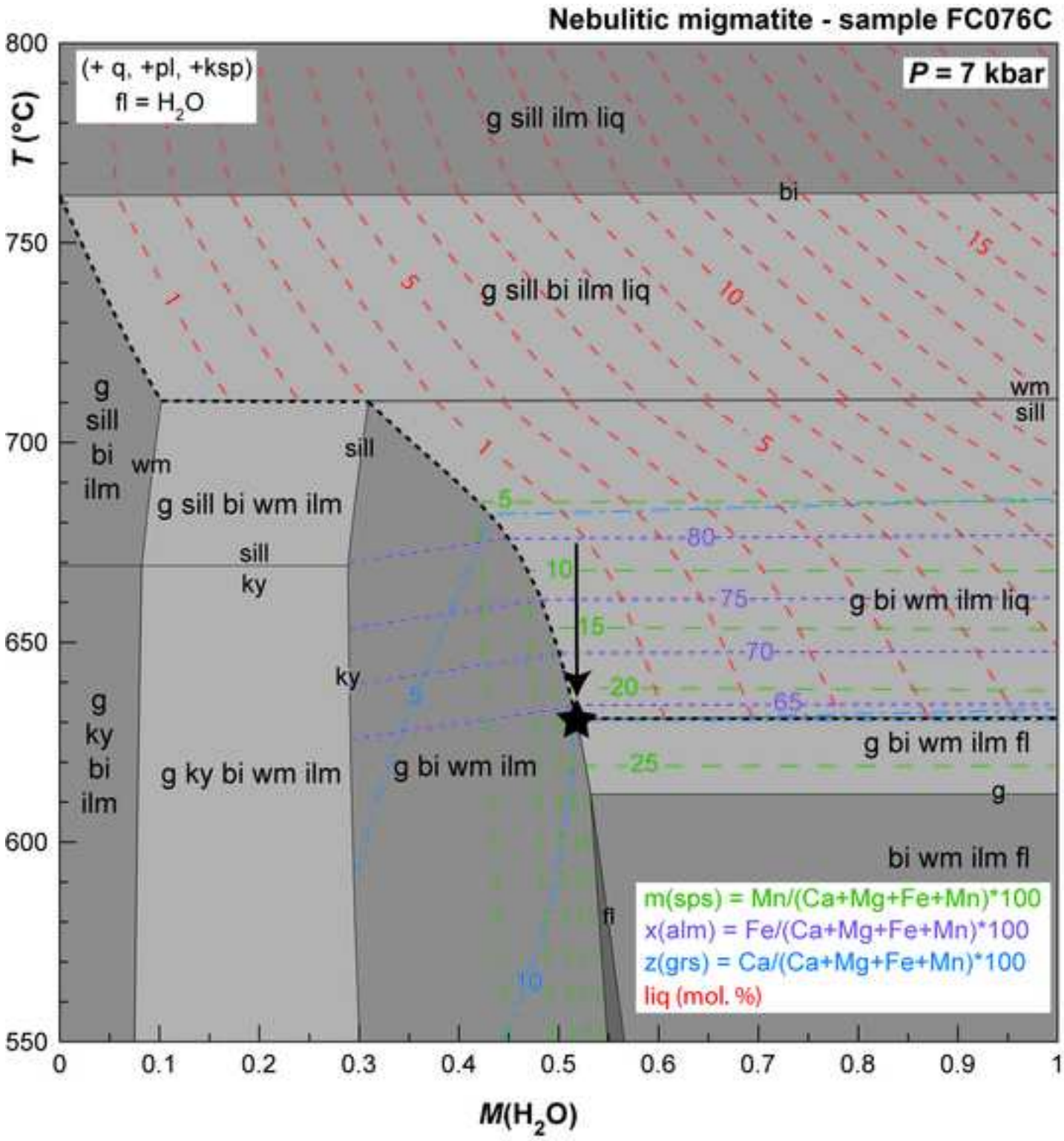

H_2O	SiO_2	Al_2O_3	CaO	MgO	FeO	K_2O	Na_2O	TiO_2	MnO	O	
0.00	81.33	8.76	0.76	0.56	1.73	3.49	3.18	0.15	0.03	0.01	$M(H_2O)$= 0
4.00	81.33	8.76	0.76	0.56	1.73	3.49	3.18	0.15	0.03	0.01	$M(H_2O)$= 1

Fig.13

Click here to access/download;Figure;Fig13.tif

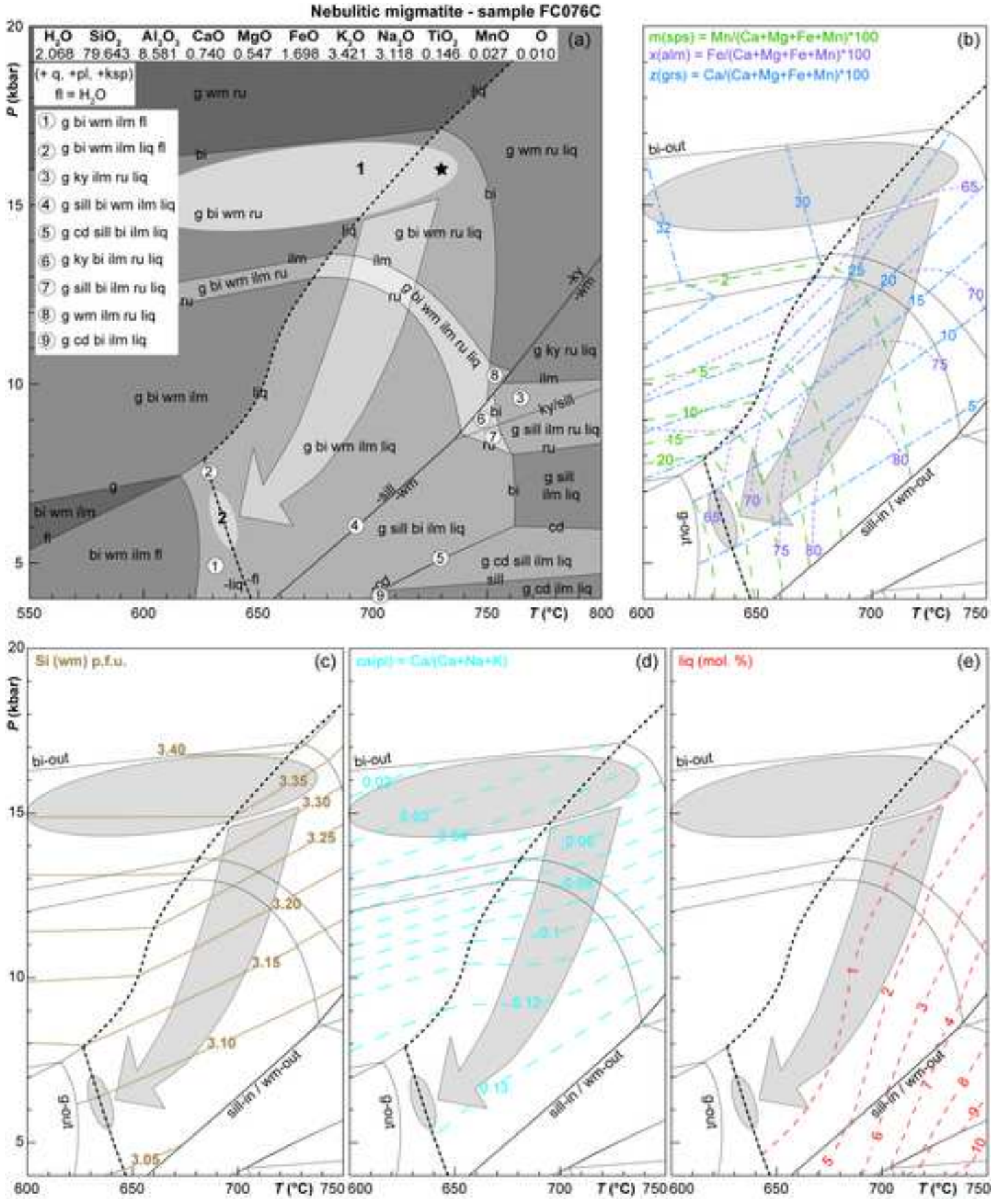

Fig.14

Click here to access/download;Figure;Fig14.tif

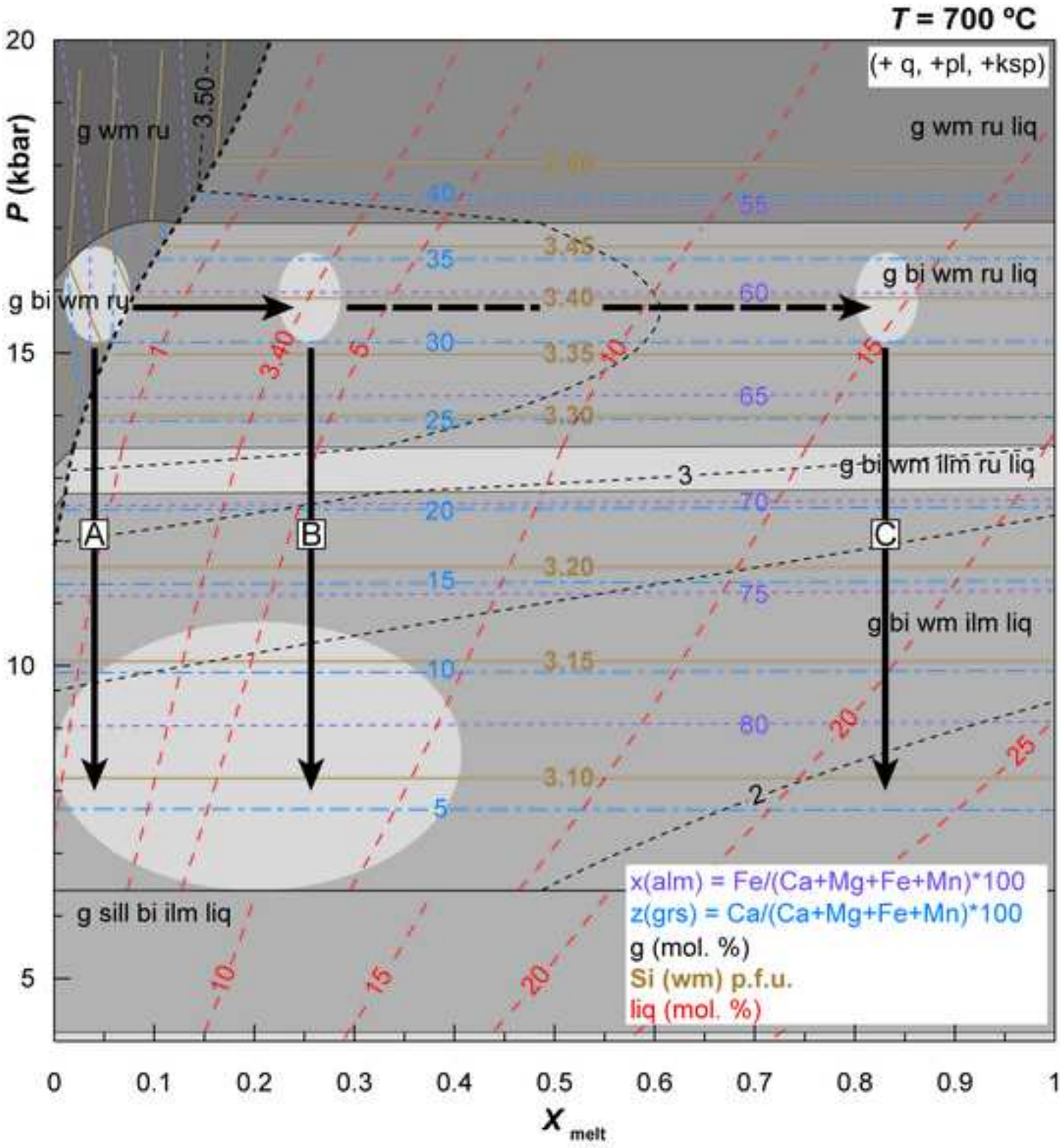

H_2O	SiO_2	Al_2O_3	CaO	MgO	FeO	K_2O	Na_2O	TiO_2	MnO	O	
1.65	79.983	8.618	0.743	0.549	1.705	3.436	3.131	0.147	0.028	0.01	$X = 0$
9.055	73.530	8.203	0.640	0.460	1.451	3.131	3.383	0.118	0.022	0.008	$X = 1$

Fig.15

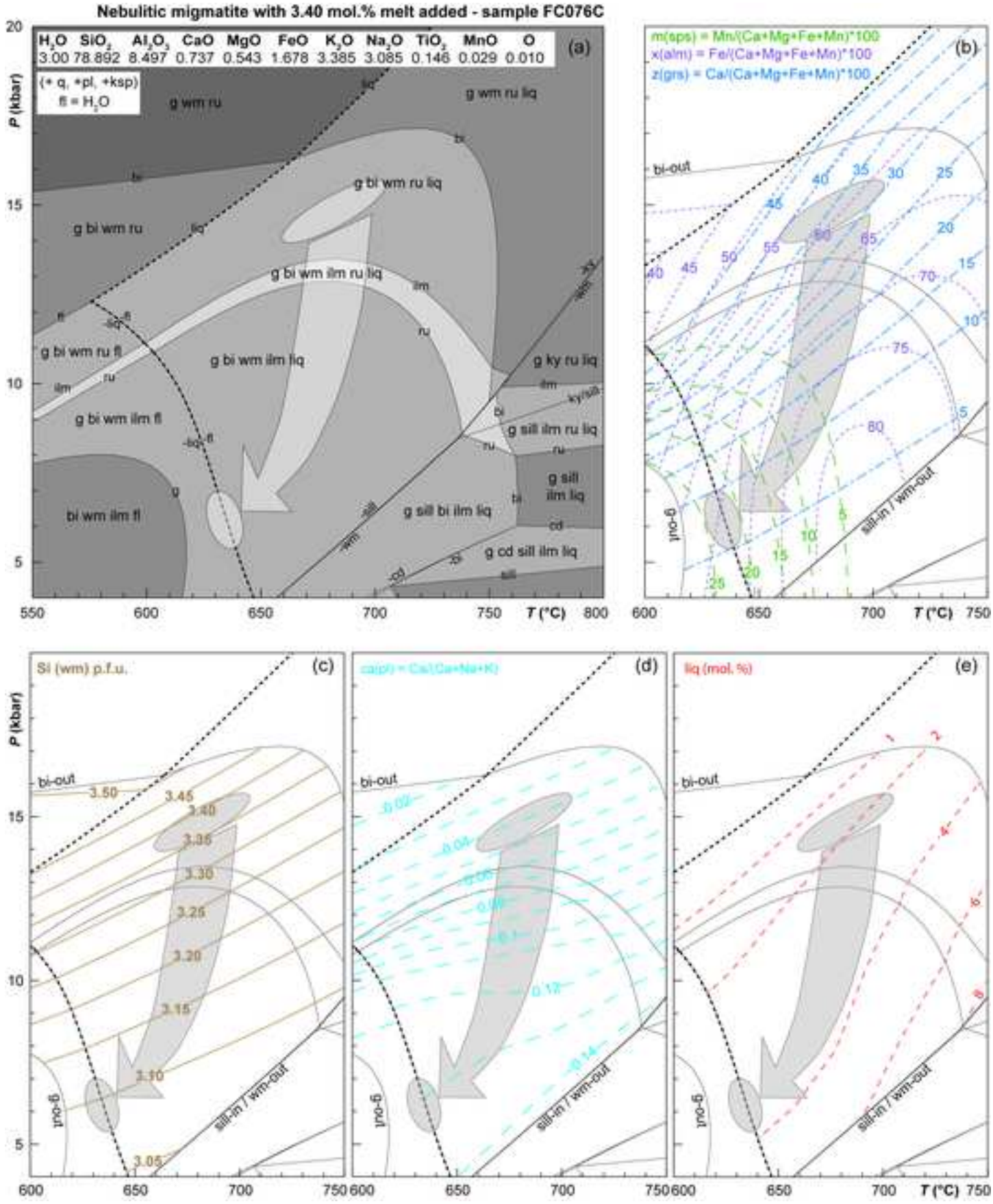

Fig.16

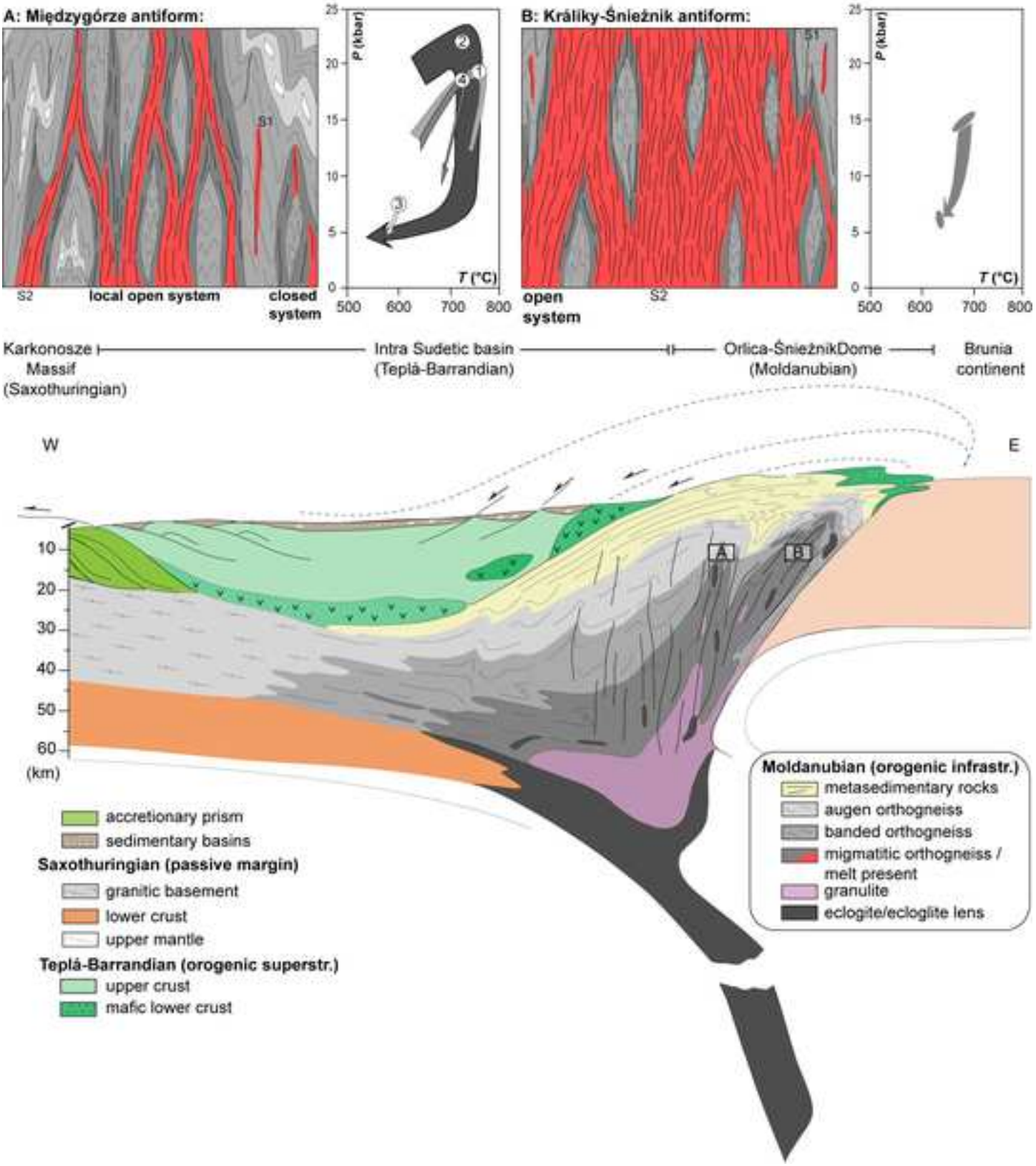

Table 1

Table 1. Representative analyses of feldspar.

Rock type	Augen-banded type II									
Sample	FC076B	FC076B	FC076B	FC076B	FC076B	FC076B	FC076B	FC076B	FC076B	FC076E
Layers	pl			kfs				q		
Position	pl_core	pl_rim	kfs_int	kfs	pl_core	pl_rim	pl film	pl film	kfs_int	pl_core
Analysis	279	280	275	319	321	305	318	328	325	pl_29
Spot										22
wt% oxide										
SiO2	66.10	67.51	65.37	65.41	65.94	67.96	70.05	64.45	65.69	64.18
TiO2	0.00	0.00	0.00	0.00	0.01	0.00	0.00	0.00	0.01	0.02
Cr2O3	0.00	0.00	0.00	0.00	0.00	0.00	0.00	0.02	0.02	0.00
Al2O3	21.25	20.14	18.27	18.28	21.49	20.22	19.06	21.98	18.10	21.33
FeO	0.00	0.01	0.01	0.01	0.01	0.04	0.00	0.00	0.00	0.00
MnO	0.00	0.00	0.00	0.00	0.00	0.00	0.00	0.01	0.00	0.00
MgO	0.01	0.00	0.01	0.01	0.00	0.00	0.01	0.00	0.01	0.01
CaO	2.47	1.29	0.00	0.03	2.37	0.99	1.21	3.40	0.02	2.92
Na2O	10.21	11.20	0.98	1.34	10.44	11.01	10.14	9.54	1.21	9.55
K2O	0.34	0.14	15.30	14.71	0.32	0.16	0.13	0.15	12.49	0.26
Total	100.39	100.29	99.94	99.78	100.58	100.37	100.59	99.549	97.54	98.268
Cations										
Si	2.90	2.95	3.02	3.02	2.88	2.97	3.08	2.86	3.12	2.88
Ti	0.00	0.00	0.00	0.00	0.00	0.00	0.00	0.00	0.00	0.00
Cr	0.00	0.00	0.00	0.00	0.00	0.00	0.00	0.00	0.00	0.00
Al	1.10	1.04	0.99	0.99	1.11	1.04	0.99	1.15	1.01	1.13
Fe	0.00	0.00	0.00	0.00	0.00	0.00	0.00	0.00	0.00	0.00
Mn	0.00	0.00	0.00	0.00	0.00	0.00	0.00	0.00	0.00	0.00
Mg	0.00	0.00	0.00	0.00	0.00	0.00	0.00	0.00	0.00	0.00
Ca	0.12	0.06	0.00	0.00	0.11	0.05	0.06	0.16	0.00	0.14
Na	0.87	0.95	0.09	0.12	0.88	0.93	0.86	0.82	0.11	0.83
K	0.02	0.01	0.90	0.87	0.02	0.01	0.01	0.01	0.76	0.01
Total	5.00	5.00	5.00	5.00	5.00	5.00	5.00	5.00	5.00	5.00
an	0.12	0.06	0.00	0.00	0.11	0.05	0.06	0.16	0.00	0.14
ab	0.87	0.93	0.09	0.12	0.87	0.94	0.93	0.83	0.13	0.84
or	0.02	0.01	0.91	0.88	0.02	0.01	0.01	0.01	0.87	0.02

Banded type II										
FC076E	FC076E	FC076E	FC076E	FC076E	FC076E	FC076E	FC076E	FC076E	FC076E	FC076E
pl			big-euhedral pl					kfs		
pl_rim	kfs core	kfs rim	pl_core	pl_rim	pl_myrm	kfs_ant	kfs_int	kfs_core	kfs_rim	pl_film
pl_27	kfs_22	kfs_26	pl_1	pl_16	pl_13	kfs_2	kfs_9	kfs_30	kfs_30	pl_36
19	24	28	4	34	31	2	22	38	44	48
64.03	64.03	63.97	63.36	64.54	63.50	64.19	64.13	64.13	63.78	78.65
0.00	0.00	0.00	0.00	0.00	0.00	0.00	0.00	0.01	0.01	0.00
0.00	0.00	0.00	0.00	0.00	0.00	0.00	0.00	0.00	0.00	0.00
21.48	18.22	18.10	22.08	21.32	21.84	18.41	18.12	18.22	18.04	12.79
0.00	0.01	0.00	0.00	0.06	0.04	0.04	0.02	0.02	0.00	0.06
0.00	0.00	0.00	0.02	0.00	0.00	0.00	0.01	0.00	0.00	0.01
0.00	0.01	0.01	0.00	0.00	0.01	0.00	0.00	0.00	0.00	0.00
3.05	0.02	0.00	3.75	2.90	3.32	0.02	0.02	0.04	0.01	0.31
9.57	1.17	0.66	8.99	9.51	9.31	1.08	0.79	1.30	0.67	8.17
0.17	15.38	16.19	0.19	0.19	0.29	15.57	15.84	15.20	16.28	0.09
98.29	98.83	98.93	98.39	98.52	98.30	99.31	98.93	98.93	98.78	100.07
2.87	2.98	2.98	2.85	2.89	2.85	2.97	2.99	2.98	2.98	3.57
0.00	0.00	0.00	0.00	0.00	0.00	0.00	0.00	0.00	0.00	0.00
0.00	0.00	0.00	0.00	0.00	0.00	0.00	0.00	0.00	0.00	0.00
1.14	1.00	0.99	1.17	1.13	1.16	1.01	1.00	1.00	0.99	0.68
0.00	0.00	0.00	0.00	0.00	0.00	0.00	0.00	0.00	0.00	0.00
0.00	0.00	0.00	0.00	0.00	0.00	0.00	0.00	0.00	0.00	0.00
0.00	0.00	0.00	0.00	0.00	0.00	0.00	0.00	0.00	0.00	0.00
0.15	0.00	0.00	0.18	0.14	0.16	0.00	0.00	0.00	0.00	0.01
0.83	0.11	0.06	0.78	0.83	0.81	0.10	0.07	0.12	0.06	0.72
0.01	0.91	0.96	0.01	0.01	0.02	0.92	0.94	0.90	0.97	0.00
5.00	5.00	5.00	5.00	5.00	5.00	5.00	5.00	5.00	5.00	5.00
0.15	0.00	0.00	0.19	0.14	0.16	0.00	0.00	0.00	0.00	0.02
0.84	0.10	0.06	0.80	0.85	0.82	0.10	0.07	0.11	0.06	0.97
0.01	0.90	0.94	0.01	0.01	0.02	0.90	0.93	0.88	0.94	0.01

		Schlieren migmatite							
FC076E	FC076E	FC076J	FC076J	FC076J	FC076J	FC076J	FC076J	FC076J	FC076J
q		big-euhedral pl			kfs preserved			mixing phases	
kfs_core	kfs_rim	pl_core	pl_rim	kfs_ant	kfs_core	kfs_rim	kfs_core	kfs_rim	pl_core
kfs_32	kfs_32	pl+kfs	pl+kfs	pl+kfs	kfs_1	kfs_1	kfs_3	kfs_3	pl_11
55	50	94	108	96	118	137	19	22	50
63.69	63.64	65.66	65.56	65.86	65.50	65.42	65.10	65.02	65.34
0.00	0.00	0.00	0.01	0.00	0.00	0.00	0.00	0.00	0.00
0.00	0.00	0.00	0.00	0.00	0.00	0.00	0.00	0.00	0.00
18.20	18.07	21.97	22.22	18.62	18.78	18.77	18.78	18.50	22.45
0.03	0.04	0.01	0.01	0.00	0.00	0.03	0.02	0.00	0.01
0.01	0.00	0.00	0.01	0.00	0.00	0.01	0.00	0.01	0.00
0.01	0.00	0.00	0.01	0.00	0.00	0.00	0.01	0.01	0.00
0.08	0.04	2.57	2.76	0.00	0.02	0.03	0.02	0.03	2.97
1.06	0.84	10.04	10.08	1.07	1.70	1.48	1.54	0.74	9.83
15.42	15.97	0.15	0.14	15.28	14.34	14.57	14.59	15.64	0.13
98.50	98.61	100.39	100.8	100.85	100.35	100.31	100.05	99.941	100.73
2.98	2.97	2.88	2.86	3.01	3.00	3.00	2.99	3.00	2.86
0.00	0.00	0.00	0.00	0.00	0.00	0.00	0.00	0.00	0.00
0.00	0.00	0.00	0.00	0.00	0.00	0.00	0.00	0.00	0.00
1.00	1.00	1.14	1.14	1.00	1.01	1.01	1.02	1.01	1.16
0.00	0.00	0.00	0.00	0.00	0.00	0.00	0.00	0.00	0.00
0.00	0.00	0.00	0.00	0.00	0.00	0.00	0.00	0.00	0.00
0.00	0.00	0.00	0.00	0.00	0.00	0.00	0.00	0.00	0.00
0.00	0.00	0.12	0.13	0.00	0.00	0.00	0.00	0.00	0.14
0.10	0.08	0.85	0.85	0.10	0.15	0.13	0.14	0.07	0.83
0.92	0.95	0.01	0.01	0.89	0.84	0.85	0.85	0.92	0.01
5.00	5.00	5.00	5.00	5.00	5.00	5.00	5.00	5.00	5.00
0.00	0.00	0.12	0.13	0.00	0.00	0.00	0.00	0.00	0.14
0.09	0.07	0.87	0.86	0.10	0.15	0.13	0.14	0.07	0.85
0.90	0.92	0.01	0.01	0.90	0.85	0.86	0.86	0.93	0.01

	Nebulitic migmatite			
FC076J	FC076C	FC076C	FC076C	FC076C
	mixing phases			
pl_rim	pl_core	pl_rim	kfs_core	kfs_rim
pl_13	pl_5	pl_13	kfs_16	kfs_16
52	98	137	131	136
64.57	63.49	64.40	64.32	63.86
0.00	0.00	0.00	0.03	0.03
0.00	0.00	0.00	0.00	0.00
22.69	21.61	21.24	18.38	18.38
0.01	0.24	0.00	0.01	0.01
0.01	0.01	0.00	0.01	0.05
0.00	0.04	0.00	0.01	0.00
3.40	3.27	2.55	0.03	0.02
9.59	9.43	10.02	1.38	0.67
0.14	0.14	0.12	14.87	16.23
100.4	98.23	98.35	99.04	99.24
2.84	2.86	2.88	2.99	2.97
0.00	0.00	0.00	0.00	0.00
0.00	0.00	0.00	0.00	0.00
1.18	1.15	1.12	1.01	1.01
0.00	0.01	0.00	0.00	0.00
0.00	0.00	0.00	0.00	0.00
0.00	0.00	0.00	0.00	0.00
0.16	0.16	0.12	0.00	0.00
0.82	0.82	0.87	0.12	0.06
0.01	0.01	0.01	0.88	0.96
5.00	5.00	5.00	5.00	5.00
0.16	0.16	0.12	0.00	0.00
0.83	0.83	0.87	0.12	0.06
0.01	0.01	0.01	0.87	0.94

Table 2

Table 2. Representative analyses of micas.

Rock type	Augen-banded type II			
Sample	FC076B	FC076B	FC076B	FC076E
Mineral_Position	bi	ph_core	ph_rim	bi
Analysis	FC076B-1_bi1	FC076B-3_mu25	FC076B-3_mu23	01A-B-bi6 Line 002
Spot	1	68	66	
wt% oxide				
SiO_2	35.45	48.66	46.78	34.75
TiO_2	1.19	0.51	0.36	2.04
Al_2O_3	20.55	32.46	34.72	18.11
FeO	23.65	2.34	2.22	27.26
MnO	0.32	0.02	0.01	0.33
MgO	4.32	1.33	0.86	4.40
CaO	0.01	0.01	0.01	0.00
Na_2O	0.08	0.32	0.43	0.09
K_2O	9.69	10.28	10.39	8.89
BaO	0.04	0.08	0.07	0.05
F	0.79	0.54	0.316	0.73
Total	96.09	96.55	96.17	96.63
Cations				
Si	2.85	3.24	3.11	2.81
Ti	0.07	0.03	0.02	0.12
Al	1.95	2.55	2.72	1.73
Fe^{3+}	0.00	0.00	0.00	0.00
Fe^{2+}	1.59	0.13	0.12	1.85
Mn	0.02	0.00	0.00	0.02
Mg	0.52	0.13	0.09	0.53
Ca	0.00	0.00	0.00	0.00
Na	0.01	0.04	0.06	0.01
K	0.99	0.87	0.88	0.92
Ba	0.00	0.00	0.00	0.00
F	0.20	0.11	0.07	0.19
Total	8.00	7.00	7.07	8.00
X_{Fe} (FeO^{+2})	0.75	0.50	0.59	0.78
X_{Fe} (FeO_{tot})	0.75	0.50	0.59	0.78
(K+Na)	1.00	0.92	0.94	0.93

	Banded typeII				
FC076E ph_core 01C-mu6 Line 007 10	FC076E ph_rim 01C-mu6 Line 010 13	FC076E ph_core 05B-mu8 Line 002 64	FC076E ph_rim 05B-mu8 Line 005 67	FC076H bi FC076H-6_bi3 72
49.06	48.44	46.92	48.04	34.07
1.37	0.85	0.51	0.68	0.99
28.85	30.21	33.33	31.08	18.53
3.36	2.98	2.59	2.96	25.73
0.01	0.02	0.02	0.06	0.35
1.61	1.38	0.90	1.26	4.39
0.00	0.01	0.01	0.01	0.02
0.24	0.32	0.43	0.33	0.07
10.16	10.32	10.21	10.09	8.61
0.07	0.05	0.07	0.05	0.00
0.574	0.36	0.28	0.43	0.57
95.32	94.93	95.27	94.98	93.33
3.34	3.29	3.16	3.26	2.83
0.07	0.04	0.03	0.03	0.06
2.32	2.42	2.64	2.49	1.82
0.00	0.00	0.00	0.00	0.00
0.19	0.17	0.15	0.17	1.79
0.00	0.00	0.00	0.00	0.02
0.16	0.14	0.09	0.13	0.54
0.00	0.00	0.00	0.00	0.00
0.03	0.04	0.06	0.04	0.01
0.88	0.89	0.88	0.87	0.91
0.00	0.00	0.00	0.00	0.00
0.12	0.08	0.06	0.09	0.15
7.00	7.00	7.00	7.00	8.00
0.54	0.55	0.62	0.57	0.77
0.54	0.55	0.62	0.57	0.77
0.91	0.94	0.93	0.92	0.92

Schlieren migmatite				Nebulitic migmatite
FC076H	FC076H	FC076C	FC076C	FC076C
ph_core	ph_rim	bi	ph_core	ph_rim
04A_mu5 Line 003	04A_mu5 Line 006	05A-bi2 Line 003	05A-mu2 Line 004	05A-mu2 Line 006
102	105	125	117	119
49.64	47.10	33.86	48.50	47.78
0.59	0.23	2.72	1.40	0.63
29.03	34.67	18.12	28.67	31.07
3.27	2.23	25.84	3.44	2.87
0.03	0.03	0.30	0.01	0.02
1.85	0.88	4.28	1.64	1.29
0.01	0.00	0.00	0.03	0.01
0.28	0.45	0.06	0.28	0.33
10.24	10.23	9.76	9.91	10.01
0.06	0.01	0.00	0.04	0.04
0.63	0.24	0.74	0.49	0.37
95.63	96.07	95.67	94.40	94.42
3.36	3.13	2.76	3.33	3.26
0.03	0.01	0.17	0.07	0.03
2.32	2.72	1.74	2.32	2.50
0.00	0.00	0.00	0.00	0.00
0.19	0.12	1.76	0.20	0.16
0.00	0.00	0.02	0.00	0.00
0.19	0.09	0.52	0.17	0.13
0.00	0.00	0.00	0.00	0.00
0.04	0.06	0.01	0.04	0.04
0.88	0.87	1.02	0.87	0.87
0.00	0.00	0.00	0.00	0.00
0.14	0.05	0.19	0.11	0.08
7.00	7.00	8.00	7.00	7.00
0.50	0.59	0.77	0.54	0.56
0.50	0.59	0.77	0.54	0.56
0.92	0.92	1.02	0.91	0.91

FC076C ph_core 05A-mu1 Line 004 74	FC076C ph_rim 05A-mu1 Line 006 76
47.39	46.83
0.40	0.21
32.35	33.83
3.05	2.32
0.03	0.04
1.03	0.76
0.00	0.01
0.42	0.38
10.12	10.09
0.01	0.00
0.42	0.21
95.20	94.67
3.20	3.17
0.02	0.01
2.58	2.69
0.00	0.00
0.17	0.13
0.00	0.00
0.10	0.08
0.00	0.00
0.05	0.05
0.87	0.87
0.00	0.00
0.09	0.05
7.00	7.00
0.62	0.63
0.62	0.63
0.93	0.92

Table 3

Table 3. Representative analyses of garnet.

Rock type	Augen-banded type II					Bande
Sample	FC076B	FC076B	FC076B	FC076B	FC076E	FC076E
Position	g2_core	g2_core	g2_rim	g3	g2_core	g2_rim
Analysis	g2 Line 005	g2 Line 007	g2 Line 015	FC76B-g3-p4	01B-g2 Line004	01B-g2 Line001
Spot	13	15	23	13	12	9
wt% oxide						
SiO_2	37.03	36.72	36.13	36.42	35.93	36.33
TiO_2	0.01	0.00	0.03	0.00	0.02	0.00
Cr_2O_3	0.00	0.00	0.02	n.d	0.00	0.00
Al_2O_3	20.94	20.75	20.33	20.58	20.21	20.54
FeO	30.27	31.83	28.91	32.77	32.39	29.32
MnO	4.19	4.50	8.31	7.32	6.64	8.47
MgO	0.71	0.81	0.64	0.68	0.72	0.50
CaO	6.16	4.05	3.00	2.33	2.44	2.95
Na_2O	0.00	0.02	0.02	n.d	0.03	0.02
Y_2O_3	0.06	0.09	0.13	n.d	0.36	0.36
Total	99.37	98.77	97.52	100.10	98.74	98.49
Cations						
Si	3.01	3.02	3.02	2.98	2.98	3.02
Ti	0.00	0.00	0.00	0.00	0.00	0.00
Cr	0.00	0.00	0.00	0.00	0.00	0.00
Al	2.01	2.01	2.01	1.98	1.98	2.01
Fe^{3+}	0.00	0.00	0.00	0.06	0.05	0.00
Fe^{2+}	2.06	2.19	2.02	2.18	2.20	2.03
Mn	0.29	0.31	0.59	0.51	0.47	0.60
Mg	0.09	0.10	0.08	0.08	0.09	0.06
Ca	0.54	0.36	0.27	0.20	0.22	0.26
Na	0.00	0.00	0.00	0.00	0.01	0.00
Y	0.00	0.00	0.01	0.00	0.02	0.02
Total	8.00	8.00	8.00	8.00	8.00	8.00
X_{Fe} (FeO_{tot})	0.96	0.96	0.96	0.96	0.96	0.97
alm	0.67	0.71	0.65	0.71	0.72	0.66
prp	0.03	0.03	0.03	0.03	0.03	0.02
grs	0.18	0.12	0.09	0.07	0.07	0.09
sps	0.09	0.10	0.19	0.16	0.15	0.19

X_{Fe} = Fe/(Fe+Mg); alm = Fe/(Fe+Mg+Ca+Mn); prp = Mg/(Fe+Mg+Ca+Mn); grs = Ca/(Fe+Mg+Ca+Mn); sps = M

ed type II				Schlieren migmatite
FC076E	FC076E	FC076J	FC076J	FC076J
g11_core	g11_rim	g2_core	g2_rim	g6
02B-g11 Line004	02B-g11 Line001	g2_02A Line 010	g2_02A Line 018	g6_02A Line 012
12	9	28	36	107
35.86	35.67	37.09	36.58	36.60
0.00	0.02	0.01	0.02	0.00
0.00	0.00	0.00	0.00	0.02
20.25	19.89	21.04	20.84	20.75
33.23	29.57	30.08	30.25	33.28
5.18	8.15	4.61	6.45	2.83
0.77	0.56	0.88	0.72	1.04
3.08	2.93	4.51	3.35	3.14
0.02	0.03	0.03	0.04	0.03
0.37	0.31	0.20	0.20	0.31
98.76	97.13	98.44	98.44	97.99
2.97	3.01	3.05	3.02	3.04
0.00	0.00	0.00	0.00	0.00
0.00	0.00	0.00	0.00	0.00
1.98	1.98	2.04	2.03	2.03
0.07	0.00	0.00	0.00	0.00
2.23	2.08	2.07	2.09	2.31
0.36	0.58	0.32	0.45	0.20
0.10	0.07	0.11	0.09	0.13
0.27	0.26	0.40	0.30	0.28
0.00	0.00	0.01	0.01	0.01
0.02	0.01	0.01	0.01	0.01
8.00	8.00	8.00	8.00	8.00
0.96	0.97	0.95	0.96	0.95
0.72	0.69	0.64	0.67	0.73
0.03	0.02	0.03	0.03	0.04
0.09	0.09	0.12	0.10	0.09
0.12	0.19	0.10	0.15	0.06

Mn/(Fe+Mg+Ca+Mn)

e		Nebulitic migmatite			
FC076J	FC076J	FC076C	FC076C	FC076C	FC076C
g9_core	g9_rim	g1_core	g1_rim	g2_core	g2_rim
g9_02A Line 010	g9_02A Line 002	FC76C-g1-p1	FC76C-g1-p1	FC76C-g2-p2	FC76C-g2-p2
150	142	10	1	10	2
36.58	36.51	37.40	36.74	37.29	36.68
0.00	0.01	0.00	0.00	0.00	0.00
0.00	0.01	n.d	n.d	n.d	n.d
20.68	20.40	21.05	20.80	20.98	20.67
29.32	28.36	29.59	30.32	26.80	28.86
7.42	8.34	2.01	9.01	1.96	9.40
0.69	0.49	0.67	0.42	0.55	0.40
3.07	2.88	9.29	3.06	11.79	3.97
0.05	0.06	n.d	n.d	n.d	n.d
0.22	0.24	n.d	n.d	n.d	n.d
98.03	97.27	100.00	100.34	99.37	100.00
3.04	3.06	3.00	2.99	3.00	2.99
0.00	0.00	0.00	0.00	0.00	0.00
0.00	0.00	0.00	0.00	0.00	0.00
2.03	2.02	1.99	2.00	1.99	1.99
0.00	0.00	0.00	0.01	0.02	0.02
2.04	1.99	1.99	2.05	1.78	1.95
0.52	0.59	0.14	0.62	0.13	0.65
0.09	0.06	0.08	0.05	0.07	0.05
0.27	0.26	0.80	0.27	1.02	0.35
0.01	0.01	0.00	0.00	0.00	0.00
0.01	0.01	0.00	0.00	0.00	0.00
8.00	8.00	8.00	8.00	8.00	8.00
0.96	0.97	0.96	0.98	0.96	0.98
0.64	0.61	0.66	0.68	0.59	0.64
0.03	0.02	0.03	0.02	0.02	0.02
0.09	0.08	0.27	0.09	0.34	0.11
0.16	0.18	0.05	0.21	0.04	0.21

Table 4

Table 4. Major and Trace-element compositions (ICP-MS) of the different types of migmatitic orth

Rock type	**Augen-banded type II**	**Banded type II**		**Schlieren migmatite**		
Sample	FC076A	FC076I	FC076E	FC076D	FC076H	FC076J
Major element (wt%)						
SiO_2	74.38	72.86	74.09	73.36	75.6	73.91
TiO_2	0.15	0.22	0.19	0.17	0.2	0.19
Cr_2O_3	<0.002	0.006	0.02	<0.002	0.011	0.017
Al_2O_3	13.46	14.29	13.69	13.85	12.89	13.57
Fe_2O_3	2.15	2.04	2.25	2.02	2.05	2.35
MnO	0.03	0.03	0.03	0.03	0.03	0.04
MgO	0.31	0.39	0.33	0.33	0.32	0.34
CaO	0.78	1.13	0.87	1.06	0.79	0.83
Na_2O	3.11	3.19	2.94	3.06	2.71	2.93
K_2O	4.47	4.99	4.83	4.92	4.43	4.64
P_2O_5	0.19	0.17	0.18	0.19	0.17	0.17
LOI	0.90	0.60	0.50	1.00	0.70	0.90
Total	99.93	99.92	99.92	99.99	99.90	99.89
$Mg/(Mg+Fe_{tot}^{a})$	0.14	0.18	0.14	0.16	0.15	0.14
Na_2O+K_2O	7.58	8.18	7.77	7.98	7.14	7.57
Trace-element (ppm.)						
Rb	192.3	199.1	194.1	193.8	176.6	177.7
Sr	52.2	63.6	59.4	55.9	49.9	52.7
Ba	234.0	394.0	325.0	288.0	292.0	310.0
Cs	4.8	4.3	4.0	3.2	3.1	2.4
Th	9.2	6.9	9.5	9.5	9.3	9.2
U	2.6	2.2	2.3	2.4	2.3	2.3
Pb	7.9	2.0	3.6	1.8	2.9	2.7
V	12.0	15.0	12.0	12.0	16.0	14.0
Sc	4.0	4.0	4.0	4.0	4.0	4.0
Zn	21.0	36.0	30.0	29.0	33.0	33.0
Zr	122.7	119.7	101.4	113.3	117.7	97.9
Hf	4.1	3.8	3.2	4.0	3.8	3.3
Nb	8.9	8.4	7.1	7.8	7.0	6.9
Ta	0.8	0.7	0.6	0.5	0.5	0.4
La	6.7	7.6	11.4	15.9	10.9	15.1
Ce	26.2	20.1	31.2	35.0	31.1	32.3
Pr	2.1	1.9	2.8	4.3	2.8	3.8
Nd	7.9	7.4	9.9	15.8	9.6	13.8
Sm	2.4	2.1	2.9	4.0	2.7	3.6
Eu	0.3	0.4	0.3	0.4	0.3	0.4
Gd	3.1	3.0	3.5	4.2	3.2	3.8
Tb	0.8	0.7	0.8	0.9	0.7	0.8
Dy	5.3	4.4	5.5	6.0	5.0	5.5

Ho	1.2	1.0	1.3	1.3	1.1	1.2
Er	3.4	2.9	3.9	3.8	3.1	3.7
Tm	0.5	0.4	0.6	0.6	0.5	0.6
Yb	3.4	2.4	3.6	3.7	3.1	3.7
Lu	0.5	0.4	0.5	0.5	0.4	0.5
Y	32.2	26.3	35.7	34.3	28.4	35.6
Sum REE	63.7	54.6	78.2	96.3	74.4	88.8

[a] Total iron as FeO

ıogneiss. LOI: Loss On Ignition.

Nebulitic migmatite
FC760C
73.80
0.18
<0.002
13.49
2.09
0.03
0.34
0.89
2.98
4.97
0.19
1.00
99.96
0.16
7.95
199.4
57.7
285.0
4.1
7.9
1.7
3.2
12.0
4.0
32.0
111.0
3.8
8.2
0.5
5.1
26.2
1.7
6.7
2.2
0.3
2.9
0.8
5.6

1.3
4.1
0.7
4.2
0.6
35.5
62.3

Table 5

Table 5. Gain/loss of incompatible elements of different rocks types relative to augen-banded type II (sample

Samples Rock types	FC076E vs. FC076A Banded type II	FC076J vs. FC076A Schlieren migmatite	FC076C vs. FC076A Nebulitic migmatite
Major elements			
SiO2	-0.05	-0.02	0.04
TiO2	0.21	0.25	0.26
Cr2O3	6.16	7.40	0.05
Al2O3	-0.03	0.00	0.05
Fe2O3	0.00	0.08	0.02
MnO	-0.04	0.32	0.05
MgO	0.02	0.08	0.15
CaO	0.07	0.05	0.20
Na2O	-0.10	-0.07	0.00
K2O	0.03	0.03	0.17
P2O5	-0.10	-0.12	0.05
Trace elements			
Rb	-0.04	-0.09	0.09
Sr	0.09	0.00	0.16
Ba	0.33	0.31	0.28
Cs	-0.20	-0.51	-0.10
Th	-0.01	-0.01	-0.10
U	-0.16	-0.13	-0.31
Pb	-0.56	-0.66	-0.58
V	-0.04	0.15	0.05
Sc	-0.04	-0.01	0.05
Zn	0.36	0.55	0.60
Zr	-0.21	-0.21	-0.05
Hf	-0.25	-0.20	-0.03
Nb	-0.24	-0.23	-0.03
Ta	-0.28	-0.51	-0.34
La	0.63	1.23	-0.20
Ce	0.14	0.22	0.05
Pr	0.27	0.78	-0.14
Nd	0.20	0.73	-0.11
Sm	0.17	0.51	-0.02
Eu	0.05	0.32	0.08
Gd	0.08	0.22	0.00
Tb	0.01	0.07	0.08
Dy	-0.01	0.03	0.11
Ho	0.08	0.02	0.17
Er	0.09	0.05	0.24
Tm	0.03	0.10	0.30
Yb	0.01	0.08	0.29
Lu	0.06	0.14	0.31
Y	0.06	0.09	0.16

FC076A)